Universidad Nacional Autónoma de México
Posgrado en Ciencias de la Tierra
Instituto de Geofísica

Dynamic Source Inversion of the 2017 M_W7.1 Puebla-Morelos Earthquake

Tesis que para obtar por el grado de
Maestro
en Ciencias de la Tierra

Presenta
Aron Yuto Sho Mirwald

Director:
Dr. Víctor Manuel Cruz Atienza
Instituto de Geofísica

Ciudad de México, Agosto 2018

Resumen

El 19 de Septiembre 2017, un sismo de Magnitud 7.1 ocurrió bajo de la frontera entre los estados de Morelos y Puebla. Fue unos de los sismos de esta magnitud más cercanos de a la Ciudad de México, con una distancia epicentral de 114 kilómetros. La ciudad de México es muy vulnerable a la actividad sísmica, dado que una gran parte de la misma está situada sobre sedimentos de lago, los que tienen una amplificación de ondas sísmicas muy alta. Como consecuencia de ello fallecieron 228 personas y colapsaron 40 edificios por la moción inducida. Además, en la estación acelerográfica de Ciudad Universitaria, un sitio de roca firme, se registró la mayor medida histórica de aceleración (60 gal, dos veces mayor que en el sismo de 1985 (M8.0) de Michoacán que mató a más que diez mil personas).

El sismo de Puebla-Morelos fue un sismo de profundidad intermedia (57 km) que ocurrió dentro de la placa de Cocos. A pesar de su descubrimiento hace ya 90 años, el mecanismo físico de los sismos de profundidad intermedia (50-300 km) sigue siendo enigmático. Debajo de 50 km, la roca ya no debería de comportarse de manera frágil, debido a la alta presión litostática. En estas condiciones ¿como se producen señales sísmicas? Los grandes catálogos sugieren consistentemente que los sismos de profundidad intermedia son resultado de un deslizamiento de cizalla en un plano, por ende, debe de existir una condición especial que permite inestabilidades de cizalla debajo de dicha profundidad. Dos de los principales mecanismos propuestos son: El cambio de la presión efectiva por agua que se libera en transformaciones mineralógicas, permitiendo que la roca rompe de manera frágil (Dehydration Embrittlement) o una retroalimentación entre temperatura y viscosidad, que resulta en una deformación extremadamente localizada (Thermal Runaway).

Los sismos de profundidad intermedia han causado mucho daño a nivel global. En México, el peligro de los sismos de profundidad intermedia es comparable al peligro de sismos interplaca, por sus aceleraciones altas y por su cercanía a ciudades grandes, por ello su estudio y comprensión resulta prioritario.

El objetivo de este trabajo es obtener un modelo relativamente sencillo de la fuente del evento para entender el proceso de ruptura. Con ese fin, se hizo una inversión dinámica de la fuente sísmica. El modelo consiste en una falla elíptica, en un medio elástico y homogéneo, con una ley de fricción en la interfaz. En con-

traste a las inversiones cinemáticas, la velocidad de ruptura en cada momento se determina resolviendo las ecuaciones elastodinámicas. Estas ecuaciones, en combinación con la ley de fricción, son altamente no lineales, lo que dificulta encontrar los mejores parámetros de fuente debido al alto número de posibles soluciones y los varios mínimos locales. Se compararon tres métodos de inversión (Algoritmos genéticos, Optimización de enjambre de partículas y Evolución diferencial) que son aptos para este tipo de problemas. Considerando una función de referencia con características parecidas al problema en cuestión, se encontró que el método de Optimización de enjambre de partículas (Particle Swarm Optimization) es el que mejor reproduce las observaciones. El modelo de fuente propuesto permite evaluar la caída de esfuerzos, la geometría del evento, la velocidad de ruptura y las energías involucradas. Teniendo estos valores, se puede obtener información sobre el proceso físico de la ruptura.

La inversión del sismo de Puebla-Morelos revela que la ruptura propagó hacia el nor-oeste, dentro de la placa de cocos, con una caída de esfuerzos alto, típica de eventos de profundidad intermedia. El resultado principal es que, a pesar de la radiación fuerte en altas frecuencias, tiene una velocidad de ruptura ($v_r/v_s \sim$ 0.3-0.5) y una eficiencia radiativa ($\eta_r \sim 0.16$) muy baja, lo que apunta hacia un proceso altamente disipativo; 84 por ciento de la energía liberada en el sismo se quedó en la zona de la fuente. Varios artículos independientes llegaron a similares conclusiones recientemente, indicado que estas son características universales para sismos de profundidad intermedia. El mecanismo de Thermal Runaway explica el proceso de ruptura altamente disipativo al proponer un gasto energético muy alto en el calentamiento de la roca.

Agradecimientos

La investigación para este trabajo ha sido increiblemente interesante, y estoy orgulloso de presentar los resultados de dos años de esfuerzo. Sin embargo, he pasado por episodios desesperantes, y admito que no hubiera logrado nada sin la ayuda de muchas personas. Primero quiero agradecer a mi familia, que ha sido una fuente de inspiración importante. Luego quiero agradecer a Jan Henzgen, Raúl Corona, Dra. Elisa Fitz Díaz, Dra. Katya Rodriguez Vázquez, Dra. Vala Hjörleifsdóttir y Dr. Shri Krishna Singh, que me ayudaron con el contenido y la forma del trabajo. Muchas gracias tambíen a mi tutor Víctor Cruz Atienza, que siempre estaba dispuesto a apoyarme. Finalmente, y tal vez más importantemente, gracias por darme un segundo hogar, mis grandes amigos Ocádiz y Rojas.

Acronyms

CLVD	Compensated linear vector dipole
DE	Differential evolution
FD	Finite difference
GA	Genetic algorithm
IDE	Intermediate-depth earthquake
NZ	Nucleation zone
PSO	Particle swarm optimization
SGSN	Staggered-grid split-node

Symbols

η_r	Radiation efficiency
E_r	Radiated energy
G	Fracture energy
σ_n	Normal pressure
p	Pore pressure
μ_f	Friction coefficient
μ_s, μ_d	Static friction coefficient, dynamic friction coefficient
$\Delta\mu$	difference of static and dynamic friction coefficient
τ	Fault strength
τ_s, τ_d	Static fault strength, dynamic fault strength
D_c	Slip-weakening distance
A	Area
ΔW	total available Energy
M_0	seismic moment
M_W	Moment magnitude
μ, λ	Lamé parameters
$\boldsymbol{u}$	Displacement vector
$\boldsymbol{\sigma}$	Stress tensor
τ_c	Source half time

Contents

Chapter 1

Introduction

On September 19th 2017, two hours after the yearly earthquake drill in Mexico City, the seismic alert triggered one more time. However, this time, it was not just an exercise. Only a few seconds after the alarm started, the institute of geophysics was rocked strongly by seismic waves. After rushing out of the building, the seismology colleagues immediately began to discuss.

The short time between the start of the alert until the arrival of seismic waves indicated that the earthquake has been generated much closer to the capital than most events felt there. Epicenters of large earthquakes are usually situated along the Pacific coast, 300 km away from the city. Also, the shaking felt extraordinarily strong. The largest accelerations usually take place in areas of the city that are build upon the ancient lake, because the lake-bed sediments amplify the seismic waves strongly. The area where the university is located, on the other hand, consists of hard bedrock, in which seismic waves are not amplified. This had to mean that the city-center was hit much harder. Unfortunately, it turned out to be true. In Mexico City, 228 people died and 43 buildings collapsed, and many more were damaged. It took several weeks to recover from the shock and chaos that emerged from the earthquake that caused the strong shaking, which has been referred to as Puebla-Morelos earthquake.

From a seismological viewpoint, the Puebla-Morelos event is very interesting. It was the closest large earthquake to Mexico City, and produced the largest accelerations ever to be recorded at the national university (UNAM). The earthquake broke a part of the Cocos plate, which subducts below the North American plate. Unlike most large earthquakes, it did not occur at the interface between the two tectonic plates, but inside the subducting Cocos plate (also called slab), as shown in Figure 1.1. The intraslab earthquakes shown in Figure 1.1 are all intermediate-depth earthquakes (IDEs), which means that they occur at depths between 50 and 300 km. Explaining the occurence of IDEs is a challenge for seismologists, because the physical mechanism that causes them is still unknown. The high pressure below

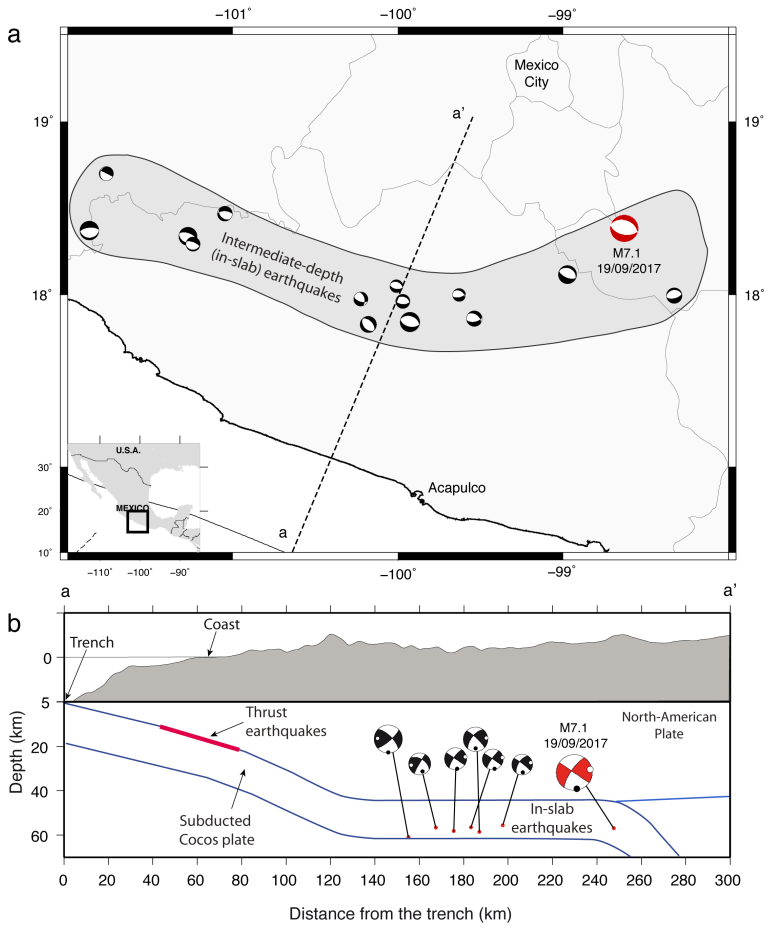

Figure 1.1: Location of Mexican intermediate-depth intraslab earthquakes after Cruz-Atienza et al. [2017]. The red beach-ball marks the Puebla-Morelos event. a: top view. Note that the Puebla-Morelos event is the closest to Mexico City. b: side view. All IDEs occur inside the subducting Cocos plate, which is marked by blue lines. The red area is where most large (thrust) earthquakes occur.

30 km does not allow the rock to break the way it normally does in shallow earthquakes. Seismologists have proposed various hypotheses about how earthquakes can nevertheless occur. It is not easy to verify these hypotheses, as IDEs are hard to access due to their depth. In comparison, the deepest borehole ever drilled reached only 12 km into the earth. Therefore, it is only possible to gather knowledge about IDEs through indirect measurements.

It is important to better understand IDEs, because they have caused much damage globally, and occur contrary to common perception relatively frequently. In Mexico, they pose a similar seismic hazard as shallow earthquakes. We investigate the Puebla-Morelos event in order to gain insights about IDEs. Our approach is to find a dynamic source model, which can explain the observations, and infer which physical mechanism could be responsible for the Puebla-Morelos event.

The structure of this work is as follows: First, we outline what is known about IDEs in Chapter 2. Then, we introduce the method that is used to generate synthetic

seismograms from a simple source model in Chapter 3. In Chapter 4, we discuss how to find the best source model. In Chapter 5, we present results of the methodology applied to the Puebla-Morelos event and discuss their relevance. Finally, we resume the work and suggest what could be done in the future in Chapter 6. The condensed content of this thesis in form of an article is provided in the appendix.

Chapter 2

Theoretical Framework: Intermediate-Depth Earthquakes

In this chapter, we first provide background information and explain the scientific interest of intermediate-depth earthquakes (IDEs). Subsequently, we give an overview of the characteristics that they have in common, and describe the currently most popular physical mechanisms which could explain their occurrence.

2.1 Background and Scientific Interest

Most earthquakes occur within the first 30 km below the earth's surface. In terms of their cause and rupture mechanism, they are relatively well-understood. Tectonic processes result in differential stresses that overcome the strength of the rock, provoking brittle fracture and frictional sliding along a narrow fault zone. For many purposes, it is adequate to model this process as a displacement discontinuity along a mathematical plane.

But earthquakes also occur at greater depth, up to 700 km [Frohlich, 2006]. In fact, around one fourth of all earthquakes occur below 60 km [Frohlich, 2006]. The first proof of such earthquakes beneath the crust was by Wadati in 1928 [Leith and Sharpe, 1936; Wadati, 1928]. From the very beginning, these earthquakes posed a mystery to seismologists since the high confining pressure at depth below 30 km should inhibit brittle fracture [Green and Houston, 1995]. One possible explanation is that deep earthquakes are caused by implosions due to mineralogical phase changes instead of frictional sliding. However, large moment-tensor catalogues consistently suggest that deep earthquakes are indeed dominated by shear slip on a fault plane [Frohlich, 1989]. Hence, there must exist a special condition which enables slip instabilities at those depths. In Section 2.3, we will discuss the principal mechanisms that have been proposed in the literature to explain this kind of earthquakes.

It is common practice to distinguish between intermediate-depth (until 300 km)

and deep earthquakes (300 - 700 km). This distinction makes sense, because it is likely that deep earthquakes have a different physical mechanism (see Section 2.2). While the lower limit of IDEs is unanimously set to 300 km depth, there are various definitions of the upper limit ranging from 30 to 70 km depth [Ranero et al., 2005; Ferrand et al., 2017]. At the Mexican subduction zone, most earthquakes are traditionally seperated into interplate and intraslab (or inslab) earthquakes, the latter ranging between 35 and 118 km depth [Singh et al., 2015; García et al., 2004]. For global analysis, we will use 50 km as a limit for shallow earthquakes, because that is the maximum depth of most thrust-zones, and the depth where aftershocks become less frequent [Frohlich, 2006].

The Global CMT catalogue from 1976 to 2018 reveals that IDEs constitute around one fifth of all earthquakes with a magnitude greater than 6. Historically, there are many IDEs that have caused great damage. Some examples are the 1939 Chile earthquake (M_S7.8) that killed over 28000 people [Frohlich, 2006] and the 1977 Romania earthquake (M_W7.5), where over 1500 people died [Fattal et al., 1977]. In Mexico, the seismic hazard from intraslab earthquakes is similar to interplate thrust earthquakes [García et al., 2004], although their frequency is much lower. This is because they are often much closer to highly populated areas than interplate earthquakes.

Therefore, it is critical to understand the underlying physical mechanism of IDEs and to assess the associated seismic hazard. There is also the hypothesis that IDEs and large thrust earthquakes are correlated [Frohlich, 2006], but this has been refuted in the Mexican subduction zone [Lemoine et al., 2002]. Knowledge of the physical mechanism of IDEs can also give insight of the composition and dynamics of the mantle.

2.2 Characteristics

What are the differences and similarities between IDEs and shallow earthquakes? Answers to this question may shed light on the physical mechanism of IDEs. In the following, we will summarize what is currently known.

IDEs occur mostly, but not exclusively, in subduction zones [Frohlich, 2006], breaking a part of the subducting plate. They tend to occur in two regions inside the subducting slab, on top of the plate interface and as much as 40 km below it [Ferrand et al., 2017]. The slab has a lower temperature than the surrounding mantle, which certainly has implications in the occurrence of IDEs. But, this fact alone cannot explain their occurrence, because of the high normal pressure. Seismologist noted early that IDEs generate surface waves of much lower amplitude and more impulsive body waves [Frohlich, 2006] than shallow earthquakes. This is not necessarily due

to their different nature, but can be accounted for by their focal depth, at which the surrounding velocity structure varies less and stimulation of elastic waves with energy concentrated near-surface is less likely [Frohlich, 2006].

In terms of their frequency-magnitude recurrence, IDEs behave as shallow earthquakes. The global b-value is around 0.9 for all types of earthquakes [Frohlich, 1989]. This means that there are many small earthquakes and only few large ones. But, there seem to be large geographical variation of b-values, and for deep earthquakes this seems to depend also on the thermal state of the slab [Wiens, 2001]. One interesting observation about IDEs is that they tend to have far less aftershocks than shallow earthquakes [Astiz et al., 1988]. No aftershocks were detected for around half of all large events [Astiz et al., 1988; Hacker et al., 2003].

On average, IDEs have larger stress drops, with a mean of 14.8 MPa [Poli and Prieto, 2016], and their source durations are shorter than shalow earthquakes. Vallée [2013] suggests that the differences in source-time duration can be explained solely by the rigidity differences, and infers that the ratio between seismic slip and rupture dimension remain equal with depth. Vallée [2013] argues that this favours a single mechanism for all earthquakes. On the other hand, there is evidence that the scaling relations with magnitude are different for IDEs [Poli and Prieto, 2014]. This is important, since we would expect different scaling relations if the physical source mechanism is different.

In order to infer the nature of IDEs, one of the most important factor is the source energy budget. The total released energy in any earthquake is divided between radiated seismic energy (E_r), fracture energy (G) and heat [Cocco et al., 2006]. With seismological methods, it is possible to infer the radiated and fracture energies. With them, the radiation efficiency can be determined:

$$\eta_r = \frac{E_r}{E_r + G}. \tag{2.1}$$

This quotient is important for the dynamics of earthquakes. Fracture energy is a macroscopic parameter that lumps together various processes such as fracturing of the fault zone and plastic deformation, but one could roughly say that it is the non-radiated energy that is dissipated in the rupture process. Around 90 percent of the fracture energy is thought to be converted to heat [Cocco et al., 2006]. That means that the radiation efficiency tells us how dissipative the rupture process is. If all the energy is radiated, the efficiency is one, and if no energy is radiated, the efficiency is zero. There is a large scatter in the efficiency data for all kind of earthquakes, probably due to the uncertainties that accompany its determination. But, on average IDEs have lower radiation efficiencies than shallow earthquakes

[Poli and Prieto, 2016; Nishitsuji and Mori, 2013], similar to tsunami-earthquakes [Kanamori and Brodsky, 2004]. However, contrary to tsunami-earthquakes, IDEs have much larger radiated energy to moment ratios [Venkataraman and Kanamori, 2004].

Kanamori and Brodsky [2004] showed that radiation efficiency correlates with rupture velocity empirically, as predicted by fracture mechanics. Therefore, determining the radiation efficiency together with the rupture velocity can give more reliable results. The problem with the rupture velocity is that most of the methods used to determine it cannot avoid the strong trade off between rupture velocity, fault area and rise-time. Nevertheless, there are some recent studies that report low radiation efficiency and low rupture velocity for IDEs [Prieto et al., 2017, 2013; Díaz-Mojica et al., 2014]. In general, it seems that low radiation efficiency and low rupture velocity correlate with warmer slabs [Poli and Prieto, 2016; Wiens, 2001], pointing towards a thermally activated mechanism.

Why is it reasonable to distinguish between deep and intermediate-depth earthquakes? The earthquake frequency falls exponentially with depth until reaching 300 km, and rises again after that [Frohlich, 1989], suggesting a change of the physical mechanism. Deep earthquakes have also some qualities that strengthen this idea: they tend to have more aftershocks than IDEs [Persh and Houston, 2004], higher radiation efficiencies [Poli and Prieto, 2016] and higher rupture velocities [Suzuki and Yagi, 2011]. Finally, the stress regime seems to change from tensional to compressional at around 300 km, although there is some variability [Frohlich, 1989]. This change could be explained by the mantle discontinuity at 670 km depth [Stein and Wysession, 2003].

Finally, let us establish why it is justified to assume that IDEs are caused by shear slip on a fault plane. The main evidence for this is that most earthquakes have double-couple radiation patterns and no resolvable isotropic moment [Frohlich, 2006]. A double-couple radiation pattern points to slip on a plane surface [Frohlich, 2006; Aki and Richards, 2002]. There is, admittedly, evidence for coupled linear vector dipole (CLVD) components for some events. These could be caused for example by simultaneous slip on two differently orientated planes. But, there are two reasons to not take this matter too seriously. While there are some events with well-resolved CLVD components, it is still debated if most IDEs have a significant CLVD component. The second reason is that the occurrence of CLVD components are only slightly different from shallow earthquakes [Frohlich, 2006].

2.3 Possible Physical Mechanisms

There are a few plausible mechanisms that were proposed for IDEs. All of them seek to explain how the generation of sudden slip under high normal stress is possible.

First, it is thought that many IDEs in subduction zones occur on pre-existent faults [Ranero et al., 2005]. This would facilitate the generation of slip, but still leaves the question on how it could be initiated under such pressure conditions. One popular hypothesis is that the effective stress is lowered by pore pressure which counteracts the normal pressure. This would reduce the shear strength of the faults following the Coulomb-Navier equation [Raleigh and Paterson, 1965]:

$$\tau = (\sigma_n - p)\mu_f, \tag{2.2}$$

where μ_f is the effective friction coefficient, σ_n is the fault normal traction, and p is the pore pressure. This model is widely accepted, because the occurrence of earthquakes spatially correlates with places where several models predict dehydration phase transformations in different subductions zones [Hacker et al., 2003]. At the laboratory scale, experiments performed show contrasting results to the question if dehydration does cause the fault to become unstable Ferrand et al. [2017]. For example, Proctor and Hirth [2015] conclude that while the weakening rate is strongly dependent on the pore fluid pressure, dehydration embrittlement is not directly causing IDEs, because of the lack of unstable slip in their experiments. Other studies have observed acoustic emissions, which where interpreted as unstable slip [Ferrand et al., 2017; Dobson et al., 2002]. Dehydration embrittlement is only viable if the volume change of the phase transition is positive, and at depths between 60 and 120 km the temperature-pressure conditions are such that the volume change is negative [Jung et al., 2004]. In a recent study, Ferrand et al. [2017] propose dehydration driven stress-transfer as an alternative mechanism. This mechanism is possible in rocks which consist of a dry phase (olivine) and a water-rich phase (antigorite) which can dehydrate, such as in the serpentized mantle. The idea here is that the water-rich phase dehydrates with a negative volume change, and alleviates the pressure on nearby dry minerals, enabling brittle fracture.

Another common hypothesis is a thermal shear instability [Prieto et al., 2012]. Instead of conventional brittle fracture, the rock is thought to experience a sudden drop in the frictional strength on the fault plane as a result of an extremely localized ductile deformation, which is likely accompanied by melting [Kanamori et al., 1998]. This is possible if the rock has an initial disturbance either in temperature or material properties [Braeck and Podladchikov, 2007]. The weaker material in the fault core deforms more than its surroundings, which in turn leads to temperature rise. Numerical simulations show that this positive feedback can lead to unstable failure

under the right conditions [Braeck and Podladchikov, 2007; Kelemen and Hirth, 2007]. Another source of evidence are recent seismological studies, which showed that the radiation efficiency (equation 2.1) is very low for some IDEs, suggesting a dissipative rupture mechanism, which was interpreted as evidence for thermal runaway [Díaz-Mojica et al., 2014; Prieto et al., 2013, 2017; Poli et al., 2016].

One problem of determining the physical mechanism is that geological observations of exhumed faults of IDEs are rare [Andersen et al., 2008]. John et al. [2009] conclude that thermal runaway can explain the different deformation patterns in a gabbro sample that was probably linked to subduction zone earthquakes. Examination on exhumed metamorphosed veins lead Plümper et al. [2017] to conclude that dehydration does result in a fluid channelization but does not cause embrittlement directly. On the other hand, Scambelluri et al. [2017] found that a fossil IDE was simply caused by release of differential stress in strong dry rocks.

It is difficult to differentiate between these mechanisms, because neither can be unambiguously linked with an observable. For example, liberated water can also weaken the rock [John et al., 2009; Plümper et al., 2017] and facilitate a thermal shear runaway instability. So, a correlation between water release due to mineralogical phase transformations and IDE locations is not enough to conclude that dehydration embrittlement is dominating the source process. On the other hand, it could be that dehydration embrittlement triggers brittle fracture on a small (microscopic) area, from where the rupture extends into ductile material, which causes the overall low efficiency of the event.

It is possible, that the phenomenon of the IDEs is not caused by a single mechanism but by a combination of the above mentioned and possibly others, yet unknown processes. It is not at all clear if a single mechanism, which explains the characteristics of all IDE types, can be determined, especially considering the wide variation of rupture characteristics.

Chapter 3

Methodology: Computation of Synthetic Seismograms: The Forward Problem

In this chapter, we describe the earthquake model we use and explore the possibility to simplify it by eliminating one parameter. Then we explain how we obtain synthetic seismograms.

3.1 Dynamic Source Model

Fault model We consider a planar fault plane embedded in a homogeneous elastic material. A friction law controls the nucleation and rupture propagation process. We use the simple linear slip-weakening law [Ida, 1972], which is depicted in figure 3.1. At a given fault point, slip is initiated when the static strength is overcome by the shear traction on the fault plane. The strength of the fault then decreases with slip linearly, until reaching its minimal value, the dynamic strength. The amount of slip where this minimum is reached is a called slip-weakening distance (D_c). To start the rupture, the traction on a small area called nucleation zone (NZ) is larger than the static strength of the rock. The rock at the NZ fails and slip is initiated. The slip then induces stresses on the edges of the NZ, which in turn can lead to further slip beyond the NZ. This rupture continues until the traction is not sufficient to break the fault. We only allow rupture on an elliptical patch by setting the strength outside to a much higher value. In figure 3.2, we show the shear traction configuration before rupture.

In total, the model consists of nine parameters. Five of them determine the elliptical fault geometry: two coordinates of the center of the ellipse (x_0, y_0), two semi-axes (a, b) and the angle of orientation (ϕ), as depectied in figure 3.3. The fault geometry can be parametrized differently , but five parameters are always needed.

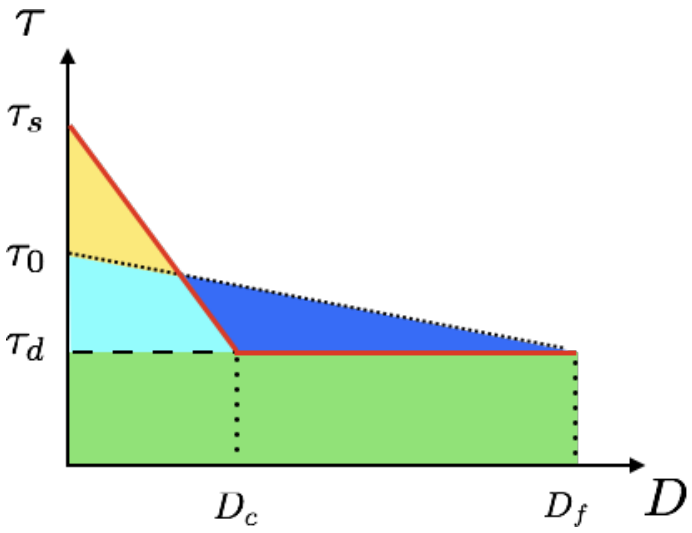

Figure 3.1: Slip-weakening model.

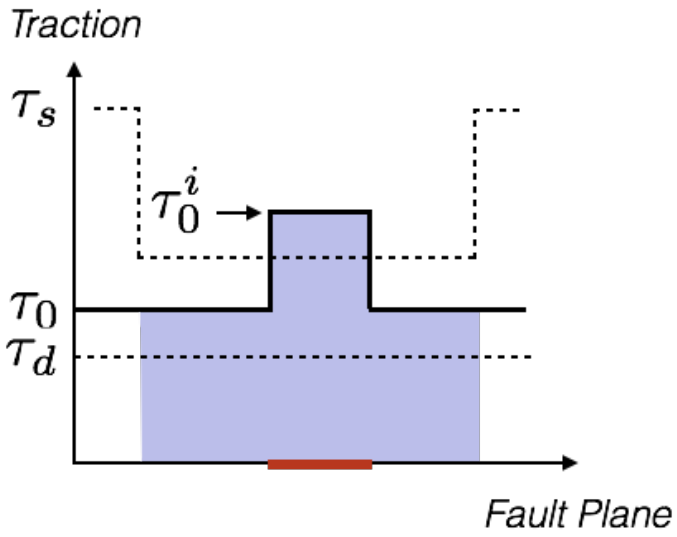

Figure 3.2: Initial shear traction along the fault (solid line). Dashed lines represent the static and dynamic strength of the fault (see fig. 3.1). The red line shows where the NZ is. The violet area marks the area where rupture is possible. Outside of that area, the static strength of the fault is set very high, not allowing the rupture to further propagate.

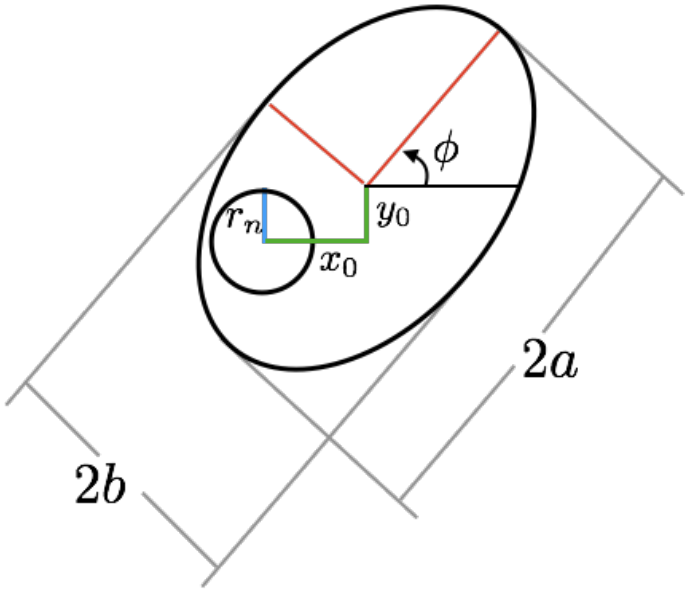

Figure 3.3: Parametrization of the ellipse.

The other four parameters are the initial traction on the elliptic patch (τ_0) , the initial traction on the NZ (τ_0^n), the slip-weakening distance (D_c), and the difference between static and dynamic friction coefficient ($\Delta\mu$). The friction coefficient is the relation between the normal traction (σ_n) and the strength of the rock, which is expressed in equation 2.2. Effectively, we are inverting the difference between dynamic and static fault strength, $\tau_s - \tau_d = \Delta\mu\sigma_n$.

Overstress One might ask if it is necessary to invert the initial traction in the NZ. Wouldn't it be enough to just set it slightly larger than the strength of the rock? Although this is right, the answer is not as simple. The problem is that although the NZ will always break, it is not guaranteed that the rupture propagates across the whole fault. The amount by which the initial traction in the NZ, τ_0^n, surpasses the strength of the fault is called overstress. In order to be physically acceptable, the overstress needs to be small. On the other hand, it is important that the rupture actually propagates. Therefore, we seek to use the smallest overstress which still initiates rupture propagation.

If the rupture propagates and breaks the whole ellipse or not depends on the initial shear traction (τ_0), the overstress ($\tau_0^n - \tau_0$), The slip-weakening distance (D_c), and the size of the NZ (A). Galis et al. [2014] studied this problem, and found that there exists a minimal area for which the rupture will be sustained, which means that it won't arrest unless forcefully stopped. The relations that predict the minimal

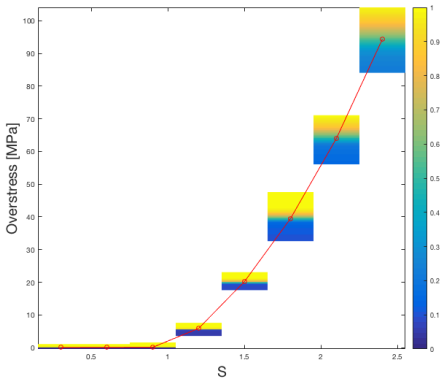

Figure 3.4: Circular rupture patch. Note that the predictions are accurate

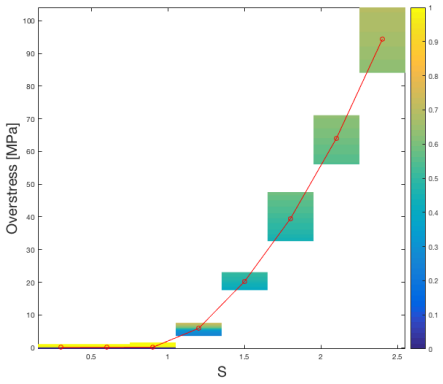

Figure 3.5: Elliptical, asymmetric rupture patch.

area are:

$$A_{min} = \frac{\pi}{16} \frac{1}{\min(f)} \frac{(\tau_s - \tau_d)^2}{(\tau_0 - \tau_d)^4} \mu^2 D_c^2, \tag{3.1}$$

$$f(x) = \sqrt{x} \left(1 + \frac{\tau_0^n - \tau_0}{\tau_0 - \tau_d} \left(1 - \sqrt{1 - 1/x^2} \right) \right).$$

Galis et al. [2014] obtained these by assuming a point load over a uniform background stress and demanding that the fracture energy surpasses a critical value. We can also use the equations 3.1 to obtain a minimal initial traction in the NZ, τ_0^n, for a fixed NZ area, A. We tested these relations using a large circular fault, and conditions that correspond to 60 km depth. Similar to Galis et al. [2014], we fix the slip-weakening distance (D_c) and the static and dynamic strength (τ_s, τ_d), and change the initial shear stress (τ_0). In figure 3.4, we show how much percentage of the circle was broken depending on the strength parameter (S) and the overstress ($\tau_0^n - \tau_0$). S is defined as the ratio between strength excess ($\tau_s - \tau_0$) and stress-drop ($\tau_0 - \tau_d$). Up to a value of S of 1.5, the prediction is successful. But, we are also interested in rupture areas which are small and non-circular. In figure 3.5, we show the results for such a geometry. Now, the theoretical prediction only holds for strength values under 1, where the overstress is very small any ways.

We conclude that although the relation holds for large rupture patches, it is not suitable for our problem. One reason is that the values of overstress that are needed are much larger than acceptable. Another is that the relation only predicts sustained rupture on an unconstrained fault plane instead of a confined ellipse.

Derived parameters From our model, we can directly derive fracture energy and radiation efficiency. In figure 3.1, the different energy contributions are shown. The

total available energy is [Cocco et al., 2006]:

$$\Delta W = \int_{\Sigma} \frac{\tau_0 - \tau_d}{2} D_f \, \mathrm{d}\Sigma, \tag{3.2}$$

where D_f is the final displacement, and the integral is carried out on the fault plane (Σ). From that energy some fraction is used to break the fault, also known as fracture energy [Cocco et al., 2006],

$$\begin{aligned} G &= \int_{\Sigma} \int_{0}^{D_f} \frac{\tau(u) - \tau_d}{2} \, \mathrm{d}u \, \mathrm{d}\Sigma, \\ &\simeq \int_{\Sigma} \frac{\tau_0 - \tau_d}{2} D_c \, \mathrm{d}\Sigma. \end{aligned} \tag{3.3}$$

The latter approximation is valid if the displacement is larger than the slip weakening distance D_c. The remaining energy is radiated in the form of seismic waves,

$$E_r = \Delta W - G \tag{3.4}$$

With equation 2.1, we can now compute the radiation efficiency. We also derive κ, a parameter that was introduced by Madariaga and Olsen [2000] and found to control the rupture behaviour,

$$\kappa = \frac{\Delta\tau^2}{\mu(\tau_s - \tau_d)} \frac{L}{D_c}, \tag{3.5}$$

where $\Delta\tau$ is the stress drop, and L is a characteristic length scale of the fault and μ is the shear modulus of the rock.

The seismic moment and the magnitude can be estimated as follows[Kanamori and Brodsky, 2004]:

$$M_0 = \mu A \overline{D_f}, \tag{3.6}$$

$$M_W = \frac{\log_{10}(M_0)}{1.5} - 6.07, \tag{3.7}$$

where $\overline{D_f}$ is the average final slip and A is the area that has experienced slip.

Finally, we can also derive the rupture velocity (v_r) on each point of the fault, utilizing the computed rupture evolution of the model. v_r is linearly connected to the radiation efficiency [Kanamori and Brodsky, 2004].

Limitations The model described above is a simplification of the actual earthquake process. Neither the linear slip-weakening model, nor the uniform traction on

the fault, nor the elliptical source shape are strictly realistic. Therefore we do not expect that the details of the model accurately represent the actual source process. Instead, we interpret the model as representing the average characteristics of the event. This is especially valid for the derived parameters, as we found that they had similar values in all models that had a good fit with the observations.

One reason for the choice of the model was simply the computational limitation and the very high non-linearity of the dynamic source problem. A larger number of parameters would result in a larger model-space, increasing the difficulty of the inversion, as discussed in section 4.1. Apart from practical limitations, a model with least possible parameters is also desirable from a theoretical point of view, if it can explain the observations satisfactory. Philosophically, natural sciences ought to adhere to the principle of parsimony (Occam's razor). Mathematically, overfitting will be a consequence of using more parameters than necessary. That is, the model with more parameters can surely reproduce the observations to a higher degree, but it would have less explanatory power. The numerous inherent uncertainties in earthquake modelling, as for example the velocity structure and the fault plane orientation, make it vulnerable to overfitting, and we conclude that a much more detailed earthquake source model is infeasible.

3.2 From the Source to the Stations

The stresses on the fault plane that are involved in the process above are calculated by solving the equation of motion. In an elastic, isotropic and homogeneous material, the equation of motion is a second order differential equation [Aki and Richards, 2002]:

$$\rho\ddot{\boldsymbol{u}} = \nabla(\lambda(\nabla \cdot \boldsymbol{u})\boldsymbol{I} + \mu(\nabla^T\boldsymbol{u} + (\nabla^T\boldsymbol{u})^T)), \tag{3.8}$$

where $\boldsymbol{u}$ is the displacement vector, $\boldsymbol{\sigma}$ is the stress-tensor, and λ and μ are the Lamé constants. Solving this equation together with the friction law is a highly non-linear problem, and there exists no analytical solution to it [Day et al., 2005; Harris et al., 2009]. One approach is to transform the equation into two coupled first-order differential equations [Madariaga et al., 1998],

$$\begin{aligned} \dot{\boldsymbol{\sigma}} &= \lambda(\nabla \cdot \boldsymbol{v})\boldsymbol{I} + \mu(\nabla^T\boldsymbol{v} + (\nabla^T\boldsymbol{v})^T), \\ \dot{\boldsymbol{v}} &= \rho^{-1}\nabla\boldsymbol{\sigma}, \end{aligned} \tag{3.9}$$

where $\boldsymbol{v} = \dot{\boldsymbol{u}}$ is the displacement velocity. These equations can be solved by approximating the temporal and spatial derivations discretely. The method we use is finite difference (FD). We use the staggered-grid slip-node (SGSN) FD method

Dalguer and Day [2007] developed, which has proven to be accurate and computationally efficient. The SGSN method approximates the temporal differentiation at the first order and the spatial differentiation at the fourth order, and incorporates the discontinuity of the fault plane by splitting the traction vector over it.

In order to further reduce the computational cost, we only solve the dynamic rupture problem in a cube with an edge length of 50 km, and use a discrete wavenumber (DWN) method to obtain the corresponding seismograms at the stations similar to Díaz-Mojica et al. [2014]. This is based on a representation theorem [Das and Kostrov, 1990]:

$$\boldsymbol{w}(\boldsymbol{x},t) = \int_0^T \int_\Sigma G(\boldsymbol{x}-\boldsymbol{x'},t-t') \cdot \boldsymbol{\Delta u}(\boldsymbol{x'},t') \; \mathrm{d}\Sigma \; \mathrm{d}t. \tag{3.10}$$

Here, $\boldsymbol{w}$ is the displacement at the position $\boldsymbol{x}$, $\boldsymbol{\Delta u}$ is the slip on the fault and G is the Green's function. In this case, the Greens function is the response of the medium to a point dislocation. We used the discrete wave number technique, AXITRA [Coutant, 1989] to calculate it, assuming a one dimensional layered velocity structure.

As for any numerical computation, it is important to find a balance between computational cost and accuracy. In our case, the controlling parameters are the spatial grid-size (Δx) and the size of the time-steps (Δt). In order to resolve the rupture process well, the ratio of grid-size to cohesion zone width should be above 4 [Dalguer and Day, 2007]. The cohesive zone, or breakdown zone, is the area of the fault plane behind the crack tip where the fault strength decreases [Dalguer and Day, 2007]. It depends on the rupture velocity and the slip evolution with time, which are controlled by the dynamic parameters. The time step is then limited by the stability limit [Dalguer and Day, 2007] $\Delta t \leq \mathrm{CFL}\Delta x/\alpha$, where CFL is the Courant-Friedrich-Lewy number.

Dalguer and Day argue that $\Delta x = 300$ is a good choice. In order to save some computation time, we would like to make the grid-size larger. We computed several different models with 300, 400 and 500 m grid size, listed in table 3.2. Although this is not a proper parametric study, we can analize the seismograms (figure 3.6) and compare them by their overstress, geometry, and slip-weakening distance (D_c). The first thing we notice is that only model a, e and f show visible differences between the different grid sizes. Model a and f have a large overstress (> 5 MPa) in common. This means that at large overstresses, a change of grid size could affect the solution strongly. But, such a large overstress is not realistic anyway. The differences of model e can be explained by the small value of the slip-weakening distance, which causes a smaller cohesion zone. We conclude, that for slip-weakening distances larger than 0.4 meters, a grid of 400 m is sufficient.

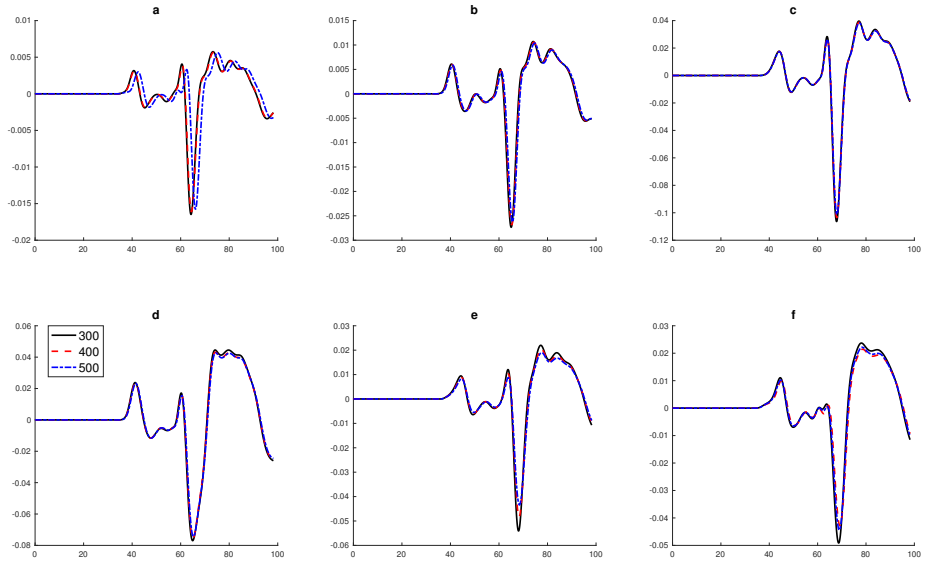

Figure 3.6: Seismograms of models listed in table 3.2.

	D_c	$\Delta\mu$	$\Delta\tau$	Overstress	Shape
Model a	0.8 m	0.03	28 MPa	11.1 MPa	asymmetrically shifted ellipse
Model b	0.9 m	0.03	28 MPa	1.1 MPa	centered circle
Model c	0.82 m	0.024	22 MPa	0.5 MPa	symmetrically shifted ellipse
Model d	0.8 m	0.03	28 MPa	11.1 MPa	centered ellipse
Model e	0.4 m	0.024	13 MPa	0.5 MPa	symmetrically shifted ellipse
Model f	0.8 m	0.024	15 MPa	5.5 MPa	symmetrically shifted ellipse

Chapter 4

Methodology: Inversion Method

In the first part of this chapter, we discuss optimization in general. Then, we compare three different optimization methods. In the last part, we define the problem that is being solved, and apply the best method we found.

4.1 Optimization

The problem of finding optimal parameters for a possibly unknown function appears in countless contexts [Storn and Price, 1997]. Some examples are the design of new products, optimization of medical analysis, investment decision making [Poli, 2008], and of course the inversion of earthquake source parameters.

In order to formulate the optimization problem properly, we first need to specify the model space (Ψ) which contains all possible parameter configurations (M). The standard approach is to design an objective function, $f(M)$ [Storn and Price, 1997], which quantifies the quality of a set of parameters contained in the model space. The optimization problem can be stated as follows [Yang, 2010]:

$$\begin{aligned} &\underset{M \in \Psi}{\text{minimize}}\ f(M), \\ &\text{subject to } \boldsymbol{g}(M) \geq 0 \text{ and } \boldsymbol{h}(M) = 0. \end{aligned} \tag{4.1}$$

That is, we are looking to find the model parameters (M) for which the function f is minimal while satisfying the constraints $\boldsymbol{g}$ and $\boldsymbol{h}$. We consider the class of such problems with a continuous model space Ψ.

Now, there are many problems with different degrees of difficulty. One common criterion is the time needed to find the optimal solution. If the problem cannot be solved in polynomial time, the problem is hard, otherwise not [Mertens, 2006]. The term polynomial time refers to the scaling of the time that is needed to compute the solution. If the time needed to solve the problem scales as a power of the number of parameters n, the time is polynomial. Roughly, one could say that

hard optimization problems cannot be solved by any deterministic method within a reasonable time limit [BoussaïD et al., 2013]. Most real-life problems are hard problems, and have often large model-spaces and an objective function with various local minima. Naturally, the goal is to find the global minimum [Torn and Zilinskas, 1989].

In order to solve hard problems, one cannot rely on the classical deterministic or linearized methods. For example, the Gradient descent is not effective because it only follows the local slope of the objective function, which makes it susceptible for being trapped in a local minimum. On the other hand, a brute-force method like grid-search is not viable because of the size of the model-space, the computational time and the uncertainty if the global minimum can be resolved by the grid. The class of methods that are designed in order to solve a wide range of hard problems approximately is called meta-heuristics [BoussaïD et al., 2013]. These methods have generally in common that they include some stochastic component, have some parameters that need to be adjusted, and are inspired by some process in nature.

There exists a vast number of different metaheuristics [Fister Jr et al., 2013], but the main principles are always exploration and exploitation. The balance between these two determines how well the algorithm will perform. Exploration is searching in new areas of the model-space to find a previously overlooked minimum, while exploitation is making use of the already obtained information, which effectively means to search in the vicinity of known minima. One common distinction is between population-based and single solution-based algorithms (e.g. simulated annealing). Population-based algorithms are generally more exploration oriented[BoussaïD et al., 2013], and are less prone to be trapped in a local minimum [Mirjalili, 2016]. As the search space of our problem is large, and we expect various local minima due to the complex nature of the problem, a population-based algorithm fits our needs better.

We will explore three algorithms: a binary genetic algorithm (GA) [Holland, 1975], particle-swarm optimization (PSO) [Eberchart and Kennedy, 1995] and differential evolution (DE) [Storn and Price, 1997]. The binary GA was previously applied to the problem of inverting the dynamic earthquake source parameters [Díaz-Mojica et al., 2014]. PSO and DE, on the other hand, are currently among the most popular optimization methods. The reason is that they show a very good performance for a large class of problems while being very easy to implement.

4.2 Comparision of Metaheuristics

No free lunch Before we start to compare different algorithms, it is important to note that it may be impossible to find one optimization algorithm that is best for

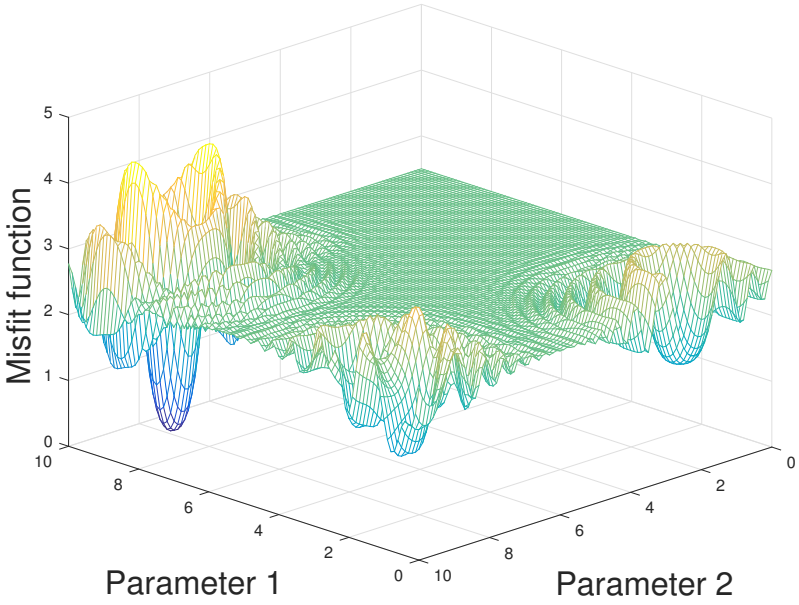

Figure 4.1: Langermann function in two dimensions.

all types of problems. Actually, it was proven mathematically that all optimization algorithms perform equally well if we average over all possible discrete functions [Yang, 2014; Burke et al., 2005]. This result is called no free lunch (NFL) theorem. If this were true, does it make sense to compare optimization algorithms at all? First, note that this theorem is valid only for discrete functions, and it is not clear if it also holds for continuous functions. Also, it is true for the average over all functions, while real world problems are a special subset, and, for example, do not include random functions [Burke et al., 2005]. Still, the NFL theorem reminds us that it is probably not possible to find a single algorithm that is superior over all others regardless of the problem. So, our approach is to compare the algorithms using a benchmark function that shares many similarities with the problem we want to solve. We chose the Langermann-5 function in nine dimensions, which is continuous, differentiable and multimodal [Jamil and Yang, 2013]. In figure 4.1, the function is shown in two dimensions.

Structure The general structure of population-based metaheuristics is very simple, as shown in diagram 4.2. First, a population of random models is generated. Then, we evaluate the objective function, also called misfit, for each of these models. The final step is to generate a new population based on the information gained from the previous generations. The main difference between the three methods is this last step. The binary GA resembles the natural evolution of species closely. The individuals (models) of the evolving population are represented by binary strings, which we could think of as genotypes. Now, the three forces of evolution are applied.

Generate random population, $X_0 = \{M_1, .., M_n\}$

DO $g = 1, ngen$

Evaluate misfit $f(M)$ of each model

Save models together with their misfit

Generate new population X_g

END DO

Figure 4.2: General scheme of how population based metaheuristics work. Here, the number of generations is limited, but it is also possible to set a ending criterion based on the misfit values.

Half of the population is discarded based on its misfit (survival of the fittest). Then, pairs of genotypes interchange information (crossover). As last step, some bits are changed randomly (mutation). We apply the same GA method as introduced by Díaz-Mojica et al. [2014].

Differential evolution also resembles natural evolution in some way. The models are represented by real valued vectors. We employ the original version of the method by Storn and Price [1997]. First, a mutant model is constructed using three random models of the previous generation.

$$\tilde{M}_i(t_{n+1}) = M_k(t_n) + \phi \left(M_l(t_n) - M_m(t_n) \right) \ , k \neq l \neq m, \tag{4.2}$$

where ϕ is a constant. k, l, and m are randomly chosen. So, the mutant model-vector is an old model-vector plus some random term generated by the difference of two other vectors. This vector is then used to generate a trial vector.

$$M_{i,j}(t_{n+1}) = \begin{cases} \tilde{M}_{i,j}(t_{n+1}), & \text{if } \xi(j) < C. \\ M_{i,j}(t_n), & \text{otherwise.} \end{cases} \tag{4.3}$$

The second index (j) indicates the parameter which is mutated. ξ is a random vector with as many elements as there are parameters, and C is a constant which we fixed as 0.5. After evaluating the objective function, only the trial vectors with better misfit values are kept.

Particle swarm optimization simulates social behaviour of animals, as for example flocks of birds [Eberchart and Kennedy, 1995]. The swarm consists of so called particles (models). The particles travel through the model space, and are assigned a position (model parameters) and a velocity. The crucial point of PSO is that each

particle remembers its best position in the past, and shares this information with the others. The rule to construct the next generation is [Shi and Eberhart, 1998a]:

$$\begin{aligned} V_i(t_{n+1}) =& \omega V_i(t_n) + \xi_1 \phi_l (M_i^{lbest} - M_i(t_n)) + \xi_2 \phi_g (M^{gbest} - M_i(t_n)), \\ M_i(t_{n+1}) =& M_i(t_n) + V_i(t_{n+1}), \end{aligned} \tag{4.4}$$

where ϕ_l and ϕ_g are constants and ξ_1 and ξ_2 are random numbers. In summary, the position of the particle is updated considering their past velocities (V_i), the globally best position of the swarm (M^{gbest}), and the best position of the particle itself (M_i^{lbest}). The velocity of the particle is reduced by the inertia (ω), which is around one for early generations and smaller for later ones. This factor is important to ensure that the algorithm does not oscillate around a minimum [Shi and Eberhart, 1998a].

Comparing the performance Since all of the methods do have a stochastic component, we need to average the results over various inversions to have a robust assessment of their capabilities. In figure 4.3 we present the misfit distribution of 200 inversions for the three algorithms. Here, we used for all methods a population of 420 and 50 generations. The binary GA had the worst performance, and virtually no inversion was able to arrive at the actual minimum. Between PSO and DE, it seems that PSO is superior for the function at hand. This is intuitive, because PSO makes use of information of the best solution of their surroundings, while DE does not. In the case of our objective function, this leads to better results. Our results are in accordance with work by Van den Bergh and Engelbrecht [2004], who compared various PSO and GA methods, and showed that the PSO method is better than GA methods for many benchmark functions.

Improving PSO It is easy to construct a function which does not reward that the models have knowledge of the best global model in the PSO method. A one-dimensional example is the function $x - 2e^{-10^4(x-1)^2}$, $x \in [0, 1]$, shown in figure 4.4. If no particle of the first generation is in the minimum at $x = 1$, the solution will never be found, because the minimum of the group will be to the left.

Another problem of the PSO is premature convergence. We address this problem with two major improvements: The premature convergence is limited by not providing, to each model, the information of the best overall model, (M_{gbest} in equation 4.4). Instead, each model only sees the best model among its nearest neighbours, as suggested by Suganthan [1999]. In this way, the swarm does not converge to a single minimum in the beginning, giving it the opportunity to explore various minima. The number of neighbours increases over the generations, so that small local minima get discarded over time. The second improvement is to randomize the whole

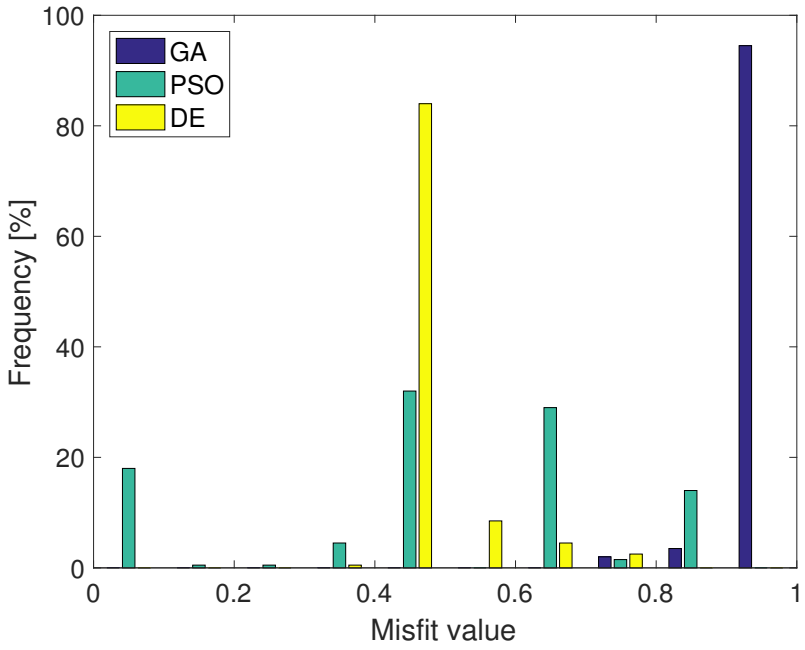

Figure 4.3: Comparison between GA, PSO and DE.

population if the best misfit does not change over a number of generations. This inhibits premature convergence, and also prevents to some degree the first problem. In figure 4.5, we show how the improved PSO compares with the original PSO, again using 200 inversions. Although the inversions only arrive at the global minimum a few more times, they never remain trapped in any minimum with values lower than 0.5, in contrast to the original PSO.

We carried out a parametric study in order to obtain the best PSO parameters for the benchmark problem. Figure 4.6, 4.7 and 4.8 show the results for the different parameters. The optimal inertia range is 1 - 0.3 (Figure 4.6), the optimal global and local weights are 0.5 and 0.6 (Figure 4.7), and the optimal initial and final population percentages used as neighbour are 10 and 50% (Figure 4.8). Although these values may depend on the problem at hand, we will employ them for the problem of dynamic source inversion.

4.3 Applying the Particle Swarm Optimization to the Dynamic Source Inversion Problem

Now, we are ready to apply the best method we found (i.e. the PSO) to the problem of the inversion of dynamic source parameters. For this purpose we adapted the inversion method introduced by Díaz-Mojica et al. [2014] to solve the problem using the PSO strategy. As explained in detail in Chapter 3, our model space consists of nine parameters: Five geometrical parameters specifying the elliptic rupture patch

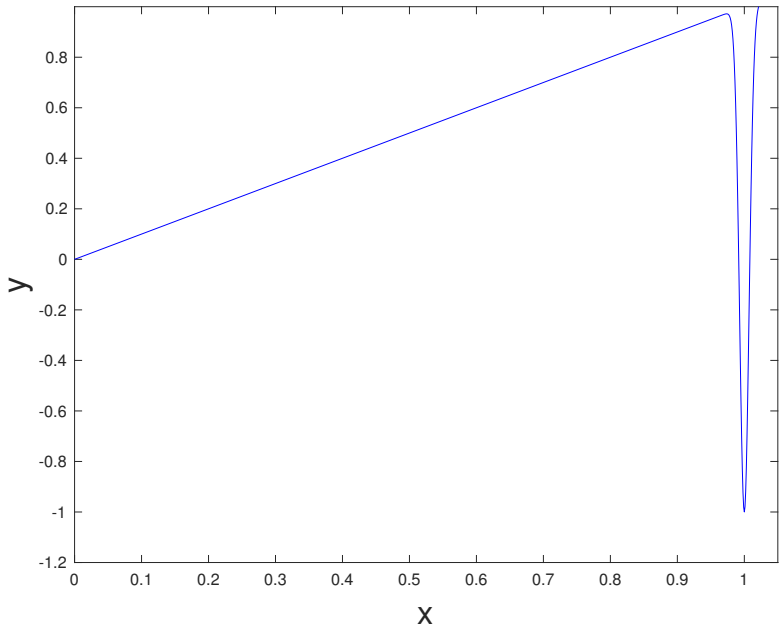

Figure 4.4: Example of a one dimensional function which is difficult to solve for the original PSO.

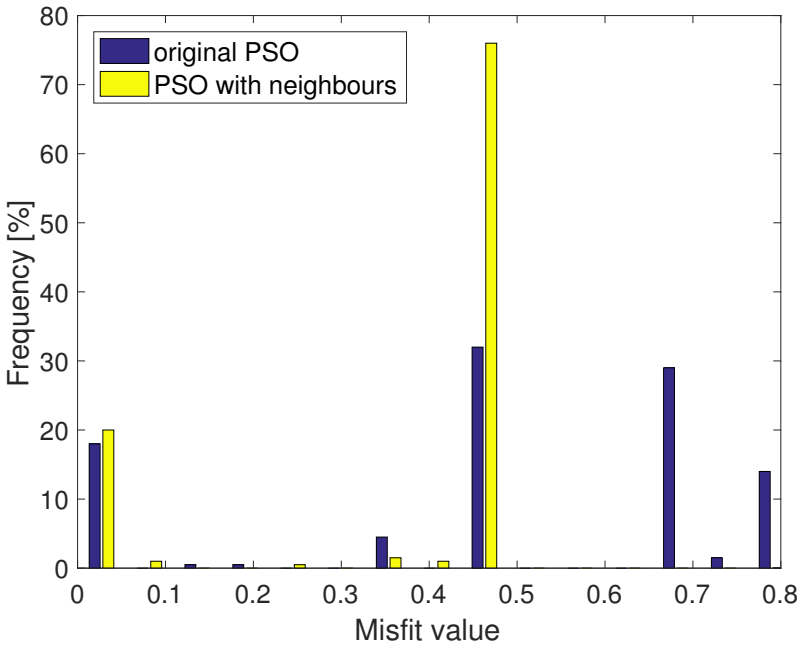

Figure 4.5: Comparison between different PSO algorithms.

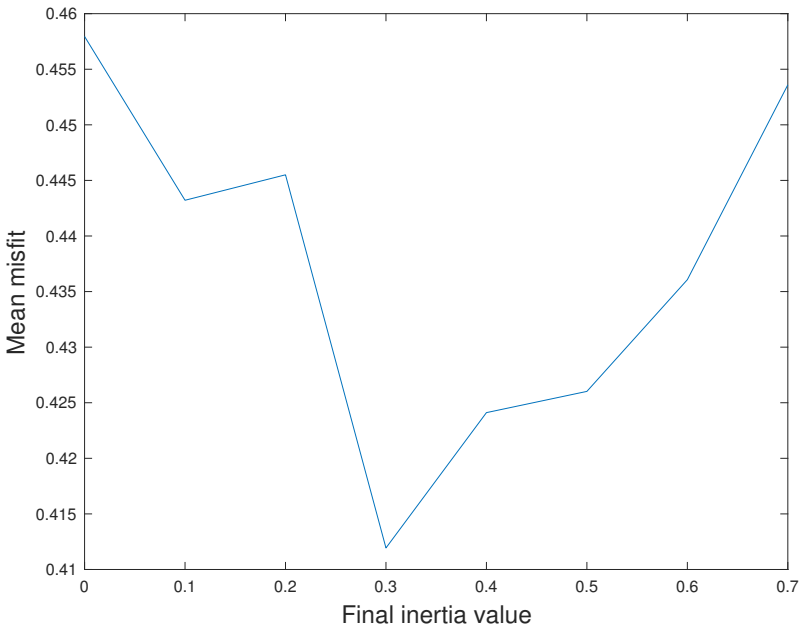

Figure 4.6: Misfit for different inertia values.

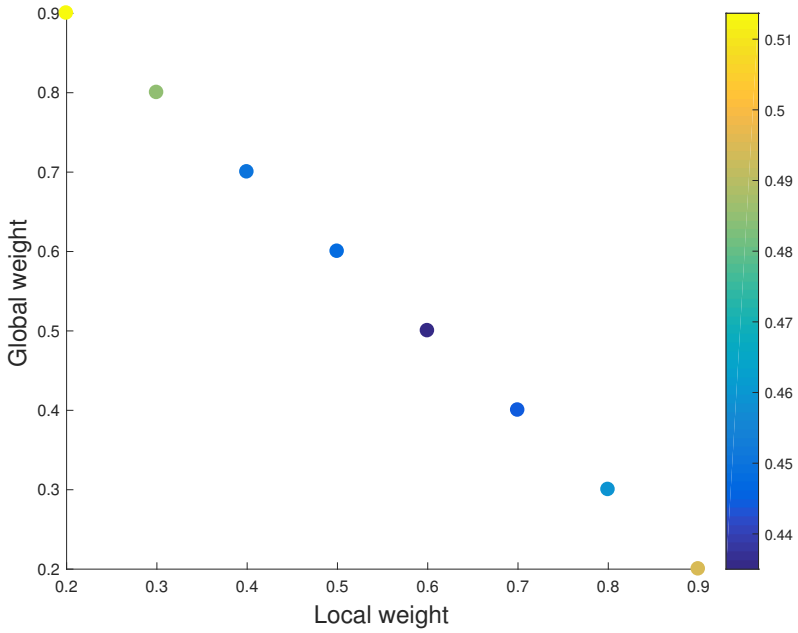

Figure 4.7: Misfit values for different weight factors. The sum of the two factors is constant- which is important in order to not affect the effect of the inertia. The colours represent the misfit of the best model achieved.

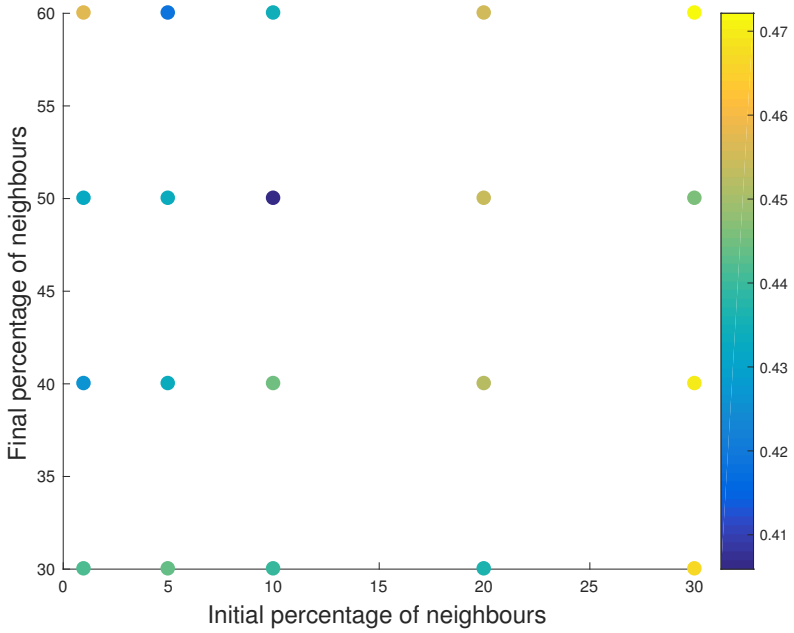

Figure 4.8: Misfit in relation to the number of neighbours that are evaluated at the beginning and at the end of the inversion. The colours represent the misfit of the best model achieved.

(a, b, x_0, y_0, ϕ), the slip-weakening distance (D_c), the initial tractions (τ_0 and τ_0^n) and the difference between static and dynamic friction coefficient ($\Delta\mu$).

Objective function From these parameters, we can compute synthetic seismograms at the stations were we also have data. The objective function (equation 4.5) is thus defined by comparing the observed and the synthetic seismograms. It consists of two parts: the first term takes into account the similarity of the waveforms, while the second term accounts for the time shift between the two signals [Díaz-Mojica et al., 2014]:

$$f = \frac{1}{3n} \sum \left(- \frac{\text{cross}(x_{obs}, x_{syn})}{\text{auto}(x_{obs}) + \text{auto}(x_{syn})} + \frac{t_{max} + \tau_c}{2\tau_c} \right), \tag{4.5}$$

where x_{obs} and x_{syn} are the observed and synthetic displacements at a given site (station), and τ_c is the source half time. The sum is carried out over the three directions (east-west, north-south and vertical) and the n stations. 'cross' and 'auto' refer to the maximum coefficients of the cross- and autocorrelation of the arguments,

calculated as follows:

$$\text{cross}(a,b) = \max_{t\in\mathbb{R}} \left(\int_{-\infty}^{\infty} a(\omega) b^*(\omega) \cdot e^{i\omega t} \mathrm{d}\omega \right), \tag{4.6}$$

$$\text{auto(a)} = \text{cross}(a,a) = \int_{-\infty}^{\infty} |a(\omega)|^2 \mathrm{d}\omega.$$

The t which maximises the first equation is exactly the t_{max} in equation 4.5.

Constraints on the parameters In order to avoid unreasonable models, it is important to implement constraints on the parameters. Specifically, we would like to exclude models with exceedingly large overstresses and models where the fault does not rupture at all or ruptures all at once. These solutions will likely be disregarded by the inversion anyway due to their bad misfit, but the computation of each model is time expensive. In terms of the model parameters, the first constraint translates into:

$$\tau_s - \tau_0 \leq 5 \text{ MPa}. \tag{4.7}$$

Here we ensure, that the initial kick (the stressdrop in the first time-step) is not larger than 5 MPa. In section 3.1 we discuss that this quantity, the overstress, should be relatively small in a realistic model.

The other two constraints can be fomulated as:

$$\tau_s - \tau_0 = \sigma_n \cdot \Delta\mu - \tau_0 > 0, \tag{4.8}$$

$$\tau_0^n - \tau_s = \tau_0^n - \sigma_n \cdot \Delta\mu > 0. \tag{4.9}$$

Looking back at figure 3.2, we can easily interpret these. If the static strength is smaller than the initial traction τ_0 on the ellipse, the whole fault will rupture in the first time step. On the other hand, if the initial traction in the NZ is smaller than the static strength, the NZ won't break at all.

There are different ways to implement the above mentioned constraints. The most common method is to penalize the objective function if the constraint is not satisfied [Parsopoulos et al., 2002]. The problem here is that no computaional time will be saved. Another approach is to reject a model if it does not satisfy the constraints and simply keep the previous model. While this is a solid approach, it makes it very difficult for the inversion to explore the edges of the model space. Instead, the idea is to adjust those models so they do satisfy the constraints, for example through confinement by dichotomy [Clerc, 2010]. We applied a more simplistic algorithm, which just adjusts one of the two parameters to satisfy the constraint. In

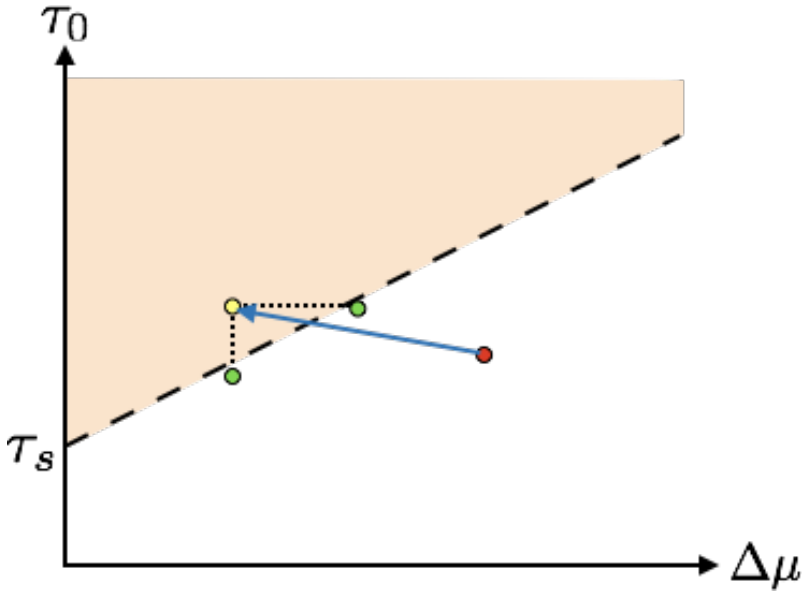

Figure 4.9: Visualization of constraints. The red particle moves into the forbidden area (yellow particle). The two possible outcomes of the constraint are representd by the green particles. Either the initial traction (τ_0) or difference of the friction parameter ($\Delta\mu$) is lowered.

order to avoid any bias, it is necessary to choose randomly which one of the two parameters is changed, as illustrated in figure 4.9.

Statistical approach Once the inversion is finished, we would like to assign an uncertainty to the best model found. There are several reasons why this is essential. First, it is very likely that the observations are contaminated by noise. Second, the model we use is very simple and may not be able to reproduce details of the observations. Third, we use many assumptions in our model which may not be accurate, as for example the wave velocity structure and the fault-plane orientation. Those factors will likely contribute to the minimum not being on the actual optimal position. Having an estimate for the uncertainties of the minimum enables us to judge its quality, and to decide if it is meaningful. It is also important to have an error estimate in order to compare the results in a physical framework with values found in other works. Without having at least some estimate of uncertainty, the result will not have as much significance.

Due to the absence of such an estimate for the PSO in the literature, we decided to proceed as follows: We gather all models which were produced by the inversion and only keep those that have a misfit at the most two times larger than the best model. From these selected models, we calculate their variances for all parameters, and take it as the uncertainty. This is possible thanks to the nature of the PSO. If one minimum is found, other individuals of the swarm are attracted to it, sampling its surroundings. Actually, we are looking at how narrow is the minimum found.

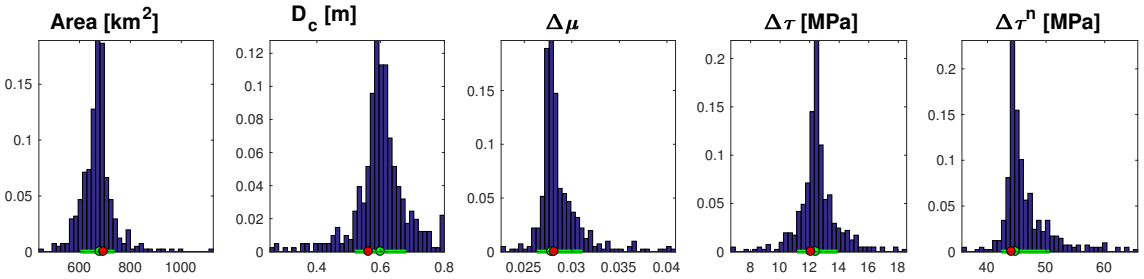

Figure 4.10: Frequency of models with a misfit smaller than $2f_{min}$. The red point is the position of the best model, the green line and point are the uncertainty and the mean value, respectively.

In figure 4.10, one example of the distribution of parameters for an inversion is shown. A weakness of this strategy is that the cut-off value for the maximum acceptable misfit used to select the models is somehow arbitrary, and our estimate of uncertainty is affected by it, unless the minimum has special properties. So, noting that the uncertainty estimates are only crude, it will at least give us some idea of how large the scatter of each parameters is and how sensitive is the model to each parameter.

Chapter 5

A Case Study: The 2017 M_W7.1 Puebla-Morelos Earthquake

In this chapter, we apply the above described methodology to the Puebla-Morelos event. We first describe the data that were used for the inversion and then present the obtained results.

5.1 Data and Focal Mechanism

The inversion was performed using accelerograms of 6 strong motion stations belonging to the National University of Mexico (UNAM) with an epicentral distance smaller than 110 km (see Figure 5.1). We selected the stations avoiding those with large site-effects, while maintaining a good azimuthal coverage. We first aligned the seismograms with the theoretical P-wave arrivals predicted by the regional velocity model of Table 5.1. The accelerograms were bandpass filtered between 0.05 and 0.15 Hz and integrated twice to obtain the displacements that were inverted. The corner frequency of the event is ∼0.08 Hz, which is consistent with the source time function duration of ∼13 s reported by the USGS. The inverted frequency band thus includes essential information of the source finiteness. We choose the upper cut-off frequency because of the simplicity of both the source model and the 1D velocity structure, that prevent us to solve for rupture details that are actually irrelevant for capturing the overall physics of the source.

Since it was not possible to determine the fault plane unambiguously using the aftershocks sequence, we inverted the source process for both auxiliary planes (Figure 5.2). The inversion yielded similar model parameters for both planes, so we decided to discuss only the results for the fault mechanism dipping to the south ($\phi = 108°$, $\delta = 47°$, $\lambda = 98°$), which yielded 20% better fits with the observed waveforms.

Table 5.1: P- and S-Velocities from Campillo et al. [1996].

Depth (km)	v_s (m/s)	v_p(m/s)	ρ (km/m^3)
0-5	3100	5370	2490
5-17	3300	5720	2600
17-45	3800	6580	2880
> 45	4700	8140	3380

5.2 Results

Due to the stochastic nature of the optimization method, we decided to run multiple inversions. Although misfit values from all inversions were of the same order, we noticed that parameters from the preferred models were different to some extend and that they are physically interdependent. As expected, larger stress-drop is generally accompanied by smaller area and larger D_c, or lower rupture velocity with larger D_c. Ruiz and Madariaga [2013] noticed similar trade-offs between the parameters for similar dynamic source inversions. However, the variation range of the preferred model parameters from our inversions are relatively small. Even more importantly, there are invariant physical parameters across the models such as the radiated energy, fracture energy, radiation efficiency, rupture velocity and rupture area. This means that, for explaining the data, all solution models share the same energy partition and rupture kinematics.

The selected models correspond to the best-fit solutions from 12 independent inversions whose misfit values are smaller than 0.15. The final solution (Table 5.2) is thus the average of these models along with their standard deviation. If the time-shift (τ_c) between the signals was zero, our misfit threshold of 0.15 implies that the second term on the right-hand side of Equation 4.5, which is known as the semblance, is smaller than 0.35. In this sense, since 0.5 is its highest possible value, our selected models explain more than about 70% of the observed waveforms. The seismograms fits are shown in Figure 5.2, where we compare the average waveforms from the selected models (black curves) along with the associated standard deviations (gray band). Despite the simplicity of the source model and the velocity structure, most of the main waveform characteristics are well reproduced, which gives confidence to our model solutions.

In Figure 5.3a we show the average final slip from the 12 selected models and the geometry of the best-fit solution whose misfit value is 0.11 (white dashed ellipse). Rupture predominantly propagates to the north-west an up-dip with an average final slip of 2.1 ± 0.3 m, which is a reasonable value for earthquakes of this size. If we project the rupture path from the NZ to the rupture left extremity into the Earth's surface, rupture directivity points roughly towards Mexico City. This could partly explain the anomalously high accelerations observed in that direction [Singh

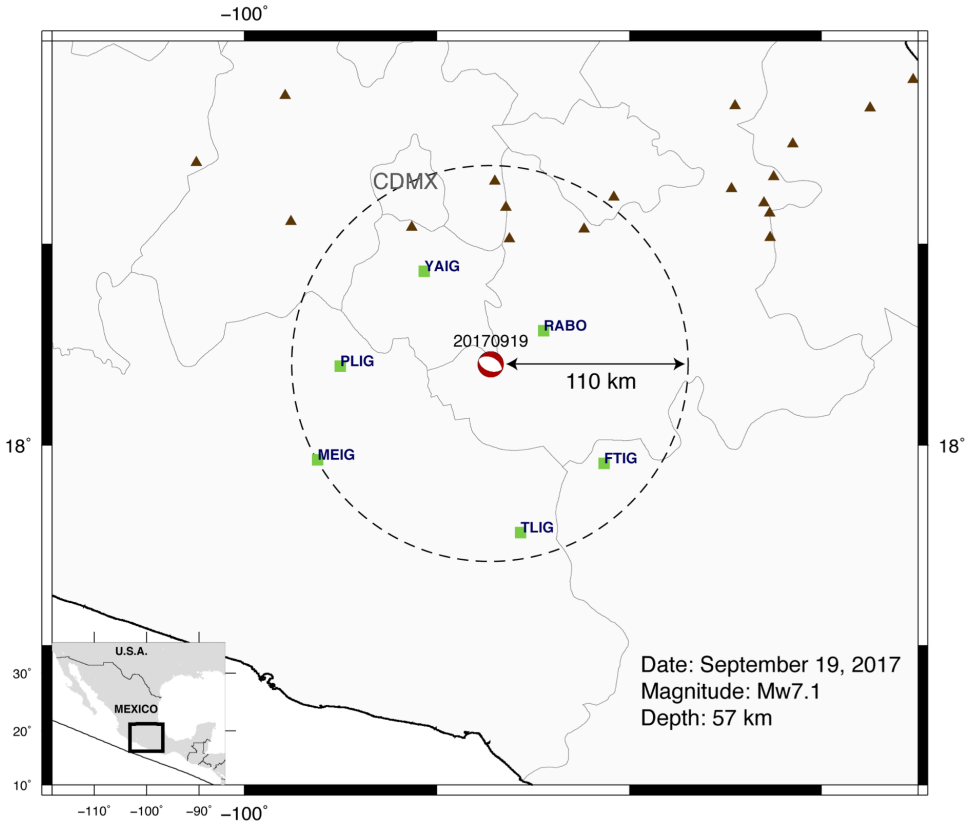

Figure 5.1: Location and focal mechanism of the Puebla-Morelos event (red beach-ball) along with the six strong motion stations that were used for the inversion. Brown triangles represent main volcanoes.

et al., 2018]. It is worth mentioning that a consistent direction of rupture directivity was found for all solutions obtained from the inversions in the other auxiliary fault plane, dipping to the north (not shown).

Although rupture velocity is remarkably low across large parts of the fault (average speed of 0.34 ± 0.04 of the shear wave speed (see Table 5.2)), it is also highly variable (Figure 5.3b). Just after nucleation, rupture reaches velocities around $0.5V_s$ along ∼10 km up-dip from the NZ and then slows down rapidly, specially along-strike, where it almost stops a few kilometers to the north-west. Rupture finally accelerates around 20 km from the NZ to reach values around $0.5V_s$ close to the north-west fault extremity.

Cracks theory predicts that the faster the rupture front, the larger is the radiation efficiency. This is shown in Figure 5.4 for the three different faulting modes (gray lines). Since fracture energy is almost constant across the fault because of our friction model, rupture speed variations should map bulk regions where radiation of seismic energy (or the seismic-moment rate) is enhanced. Figure 5.3c confirms such prediction by revealing two maximum of the peak slip-rate that spatially correlate with fault regions where V_r is maximum (compare with panel b). Consistently, the

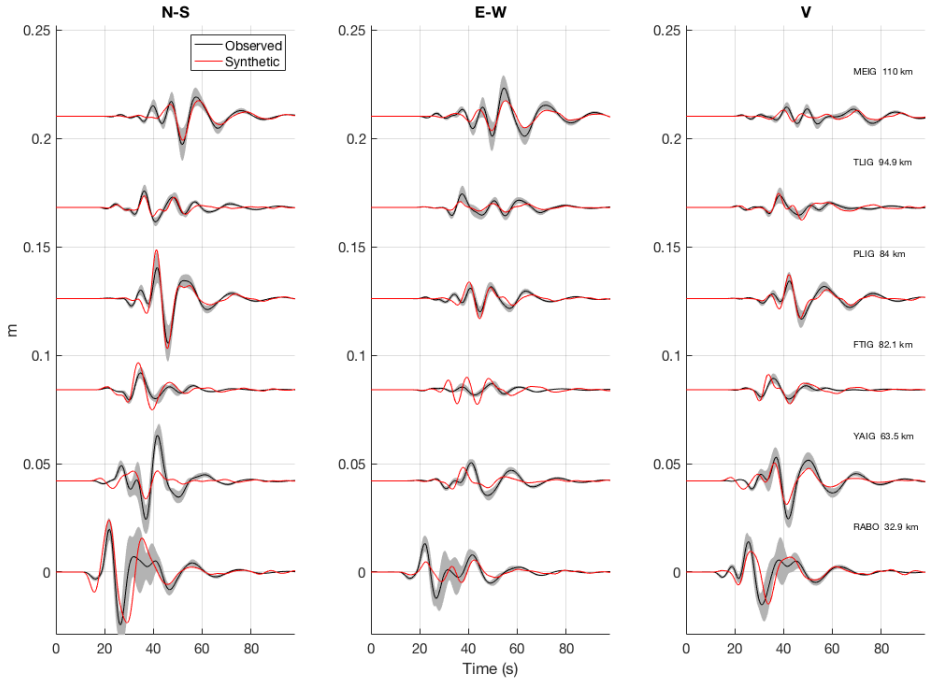

Figure 5.2: Observed and inverted seismograms. The black line is the average of all inversions, and the grey area is two times the standard deviation.

average moment rate function (Figure 5.3d) shows two bumps centered at 1 and 10 s, as well as a total source duration close to 16 s. We notice that the first peak is somehow an artefact due to the initial kick in the dynamic rupture nucleation .

The inversion yielded a stress drop of 14.9 ± 5.6 MPa, which is high compared with typical values for shallow earthquakes, but expected for IDEs in Mexico [García et al., 2004] and at a global scale with mean value of ∼15 MPa [Prieto et al., 2012; Poli and Prieto, 2016]. From the inverted parameters, we derived a radiated energy $E_r = (1.8 \pm 0.9) \cdot 10^{15}$ J, a fracture energy $G = (1.04 \pm 0.3) \cdot 10^{16}$ J and a remarkably low radiation efficiency $\eta_r = 0.16 \pm 0.09$. All the inverted and derived parameters from the inversions are reported in Table 5.2.

As compared with the magnitude M_w7.1 determined by the Mexican Servicio Sismológico Nacional (SSN) using the regional W-phase, all inversion we carried out yielded a magnitude overestimation with a mean value of $M_w 7.28 \pm 0.07$. This is likely due to lack of low frequencies below 0.05 Hz because of the bandpass filtering required for the double integration of accelerograms. We obtained the similar overestimation for synthetic inversion tests in the same frequency band, but recovered a stress drop and other derived parameters very close to the target values, so we are confident of our energy partition estimates for the actual M_w7.1 earthquake.

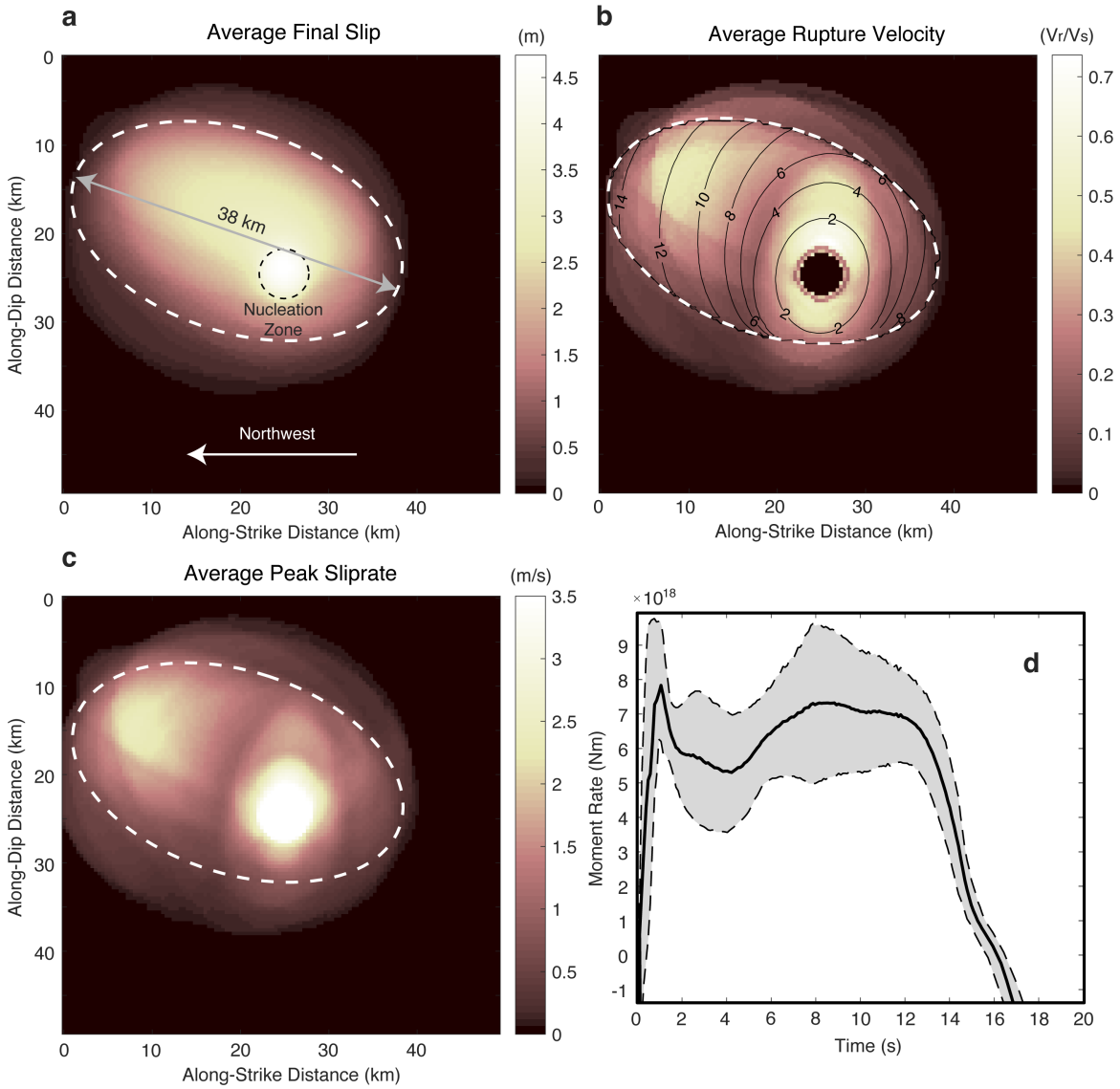

Figure 5.3: Average final slip (a), average rupture velocity normalized by the shear wave speed of 4.7 km/s along with the rupture time contours of the best-fit model (b), average peak sliprate (c) and the average moment rate function along with the standard deviation in gray (d). The dashed white ellipse depicts the geometry of the best fitting model. All models share the same nucleation zone geometry (black dashed circle).

5.3 Discussion

In agreement with the analysis of the 2001 Zumpango IDE (M_w6.5) in Guerrero, Mexico [Díaz-Mojica et al., 2014], the inversion of the Puebla-Morelos event revealed that the rupture speed ($v_r/v_s \sim 0.34$) and the radiation efficiency (η_r ~0.16) are remarkably low (Figure 5.4). Besides, as expected for most intraslab Mexican earthquakes, the stress drop ($\Delta\tau$ ~14 MPa) is relatively high. Similar results for IDEs were found in the Japan subduction zone [Nishitsuji and Mori, 2013], and more recently at a global scale [Poli and Prieto, 2016] and below the Wyoming Craton, USA, in a completely different tectonic setting [Prieto et al., 2017], suggesting that slow, inefficient source processes may predominantly characterize the rupture process of IDEs.

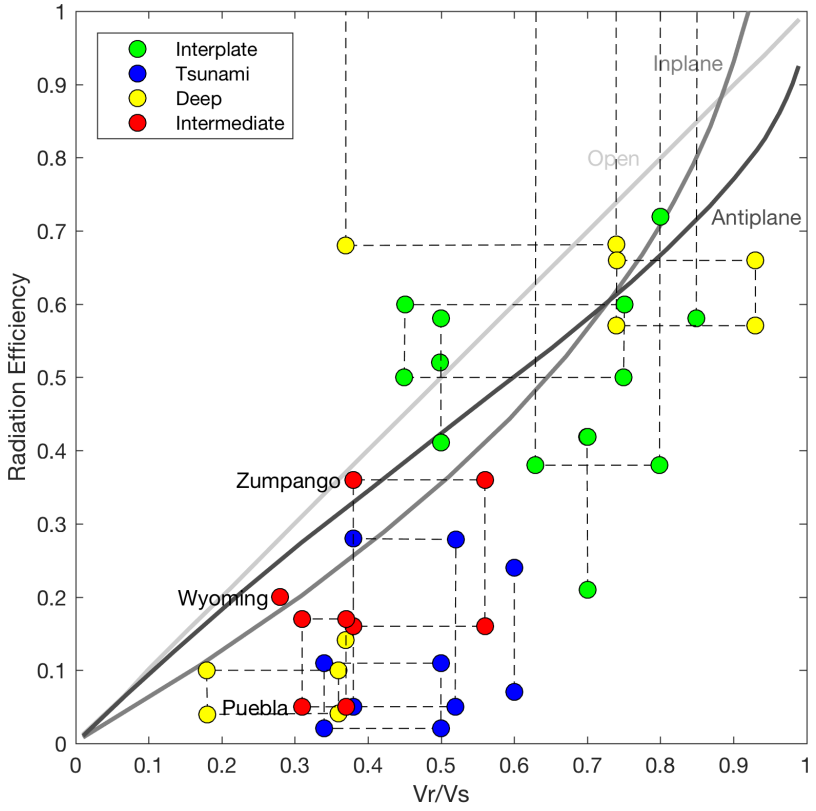

Figure 5.4: Radiation efficiency (η_r) as a function of rupture velocity (Vr) normalized by the shear wave speed (Vs) for different types of earthquakes including the Puebla-Morelos event. Reported IDEs (red dots) share the same properties as tsunami earthquakes, with very low average rupture velocity and radiation efficiency. Gray lines depict theoretical predictions for the three different deformation modes. Modified from Kanamori and Brodsky [2004].

Although such rupture properties are typical of tsunami earthquakes (see Figure 5.4), the 2017 M_w7.1 shock produced Fourier accelerations two times larger than

observed between 1 and 2 s for Mexican IDEs with similar magnitude reduced to the same hypocentral distance [Singh et al., 2018]. This means that despite the highly dissipative and slow source process, the event produced high radiation of short period waves, which is opposite to tsunami earthquakes characterized by large $M_S - M_W$ disparities. It is possible that rupture directivity contributed to this observation. However, our dynamic source model could also explain the strong shaking without rupture directivity. Considering the slip-weakening distance of 0.6 m (Table 5.2) and taking $\dot{D} = 2.0$ m/s as the mean slip-rate within the two highly-radiative fault regions shown in Figure 5.3c, the stress breakdown should have taken place in about 0.3 s. Since the peak slip rate (PSR) is approximately reached at the time when the stress drop is completed [Mikumo et al., 2003; Cruz-Atienza et al., 2009], then considering the maximum PSR values in both regions between 2.5 and 3.5 m/s, the focal particles acceleration (i.e. the peak fault accelerations) during the stress drop (i.e. at the slip onset on every fault point) should be significantly higher than 0.5g, that is between 415 and 585 *gal*. These values are consistent with observations at RABO, the closest station (hypocentral distance of 65 km), where the observed Peak Ground Acceleration was 153 *gal*.

Most interplate earthquakes have radiation efficiencies larger than 0.5 [Venkataraman and Kanamori, 2004] (Figure 5.4), which implies $G < E_r$. Since $\eta_r \sim 0.16$ for the Puebla-Morelos event, then $G = 5.8E_r$ in this case. This implies that ∼84% of the available potential energy for the dynamic process of faulting was not radiated, which means that a large amount of energy was dissipated in the focal region. Does fault-zone melting could happen due to heat production? At the very tip of the rupture (i.e. in the stress breakdown zone), the temperature rise (ΔT) is related to the specific fracture energy (G_c) as [Prieto et al., 2013]

$$\Delta T = \frac{G_c}{C\rho w}, \tag{5.1}$$

where $C \sim 1$ J/g°C is the heat capacity, ρ ∼3230 kg/m^3 and w is the fault-zone width. This equation assumes that the whole fracture energy is dissipated as heat, which is a reasonable first-order approximation considering that over 90% of the fracture energy is converted into heat [Cocco et al., 2006]. In our model, G_c (or breakdown work density, namely $W_b = G/A$) is equal to $(1.7 \pm 0.9) \cdot 10^7$ J/m^2 in average. In Figure 5.5 we show the temperature change for different fault widths predicted by Equation 5.1. According to thermal models of the subducted Cocos plate [Manea and Manea, 2011; Perry et al., 2016], the temperature of the slab where the earthquake took place is between $600 - 700$°C. The melting temperature of peridotite at those depths range between 1400° and 1800°C [Prieto et al., 2013]. Therefore, we expect melting to occur at fault widths between 0,2-1.2 cm (see figure 5.5). Field observations show that fault width is highly variable, but most fault

veins are between 0.1-3 cm[Prieto et al., 2013]. Therefore, the temperature rise at the rupture front may have indeed resulted in rock melting as suggested for other IDEs [Prieto et al., 2013]. Note that we did not include the total heat generated during the slip as Kanamori et al. [1998].

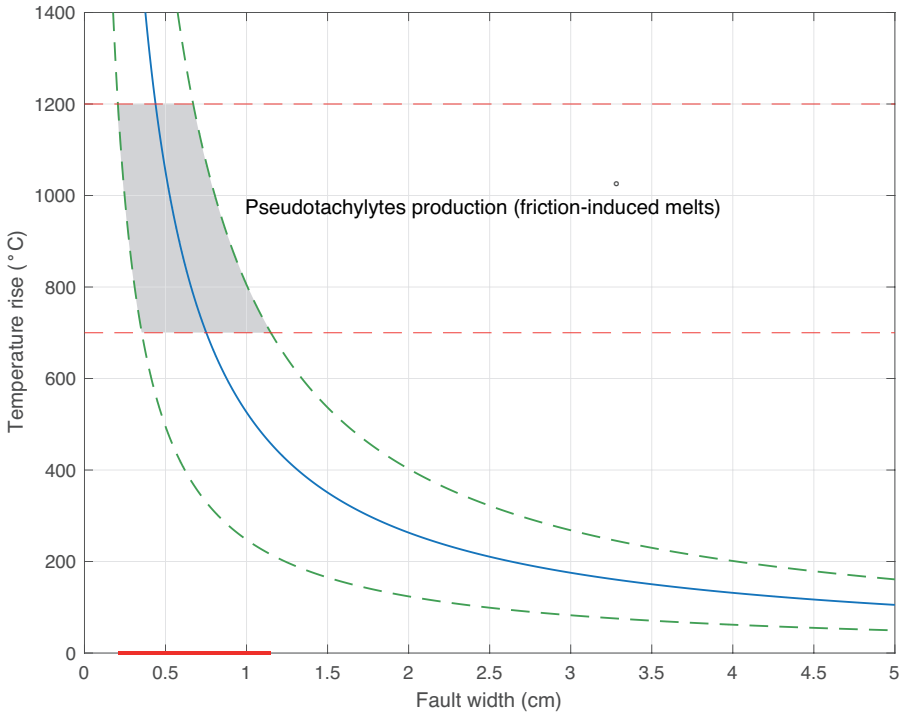

Figure 5.5: Temperature difference according to Equation 5.1.

The slow rupture velocity and low radiation efficiency of the Puebla-Morelos event (Figure 5.4) indicate that the rupture was highly dissipative. Rupture dissipation may involve different processes such as off-fault fracturing or plastic deformation. However, heat production is certainly one of the most prominent dissipative mechanisms that translate into pseudotachylytes production (friction-induced melts) in the fault-core [Di Toro et al., 2005] or heat flux [Fulton et al., 2013]. Our heat production estimate suggests that melting may have already occurred at the rupture tip, consistent with thermal runaway as the main physical mechanism driving the rupture process, as proposed by previous authors for IDEs in the Bucaramanga Nest [Prieto et al., 2013]. Dehydration from water-rich minerals could also have played a complementary role in the source process, which doesn't preclude the thermal runaway mechanism [John et al., 2009].

The hypocenter of the Puebla-Morelos event is located close to the slab segment where the subducted plate bends to sink down into the mantle (Figure 1.1). Unlike a previous kinematic source imaging of the event [Melgar et al., 2018], our preferred rupture model indicates that the active fault dips southward and that rupture prop-

Table 5.2: Inversion model-parameters ranges, and inverted and derived values.

		Range	Inverted
D_c	Slip-weakening distance	0.2-1 m	0.6 ± 0.3 m
A	Area	$80 - 1250$ km^2	713 ± 250 km^2
$\Delta\tau$	Stress-drop	0-48 MPa	14.9 ± 5.6 MPa
$\Delta\tau^n$	Stress-drop in NZ	18-78 MPa	55 ± 11 MPa
$\Delta\mu$	Difference of friction parameter	0.015 - 0.5	0.035 ± 0.007
G	Fracture energy	-	$(1.04 \pm 0.3) \cdot 10^{16}$J
E_r	Radiated energy	-	$(1.8 \pm 0.9) \cdot 10^{15}$J
κ	$\sim$ ratio of strain energy to G_c	-	1.5 ± 0.2
η_r	Radiation efficiency	-	0.16 ± 0.09
V_r	Rupture velocity	-	$(0.34 \pm 0.04)v_s$
M_w	Moment Magnitude	-	7.28 ± 0.07

agated along-strike and up-dip. Such rupture process make sense considering that (1) pre-existent plate-interface perpendicular fractures in the slab reorient with such dipping angle as the plate bends down, and (2) flexural stresses produce a reduction of the fault-normal traction (i.e. of the fault strength) towards the surface. The second argument may explain why rupture initiated in a deep focal region and then propagated up-dip to a weaker segment.

Chapter 6

Conclusion

In this work, we explored the physical mechanism of the M_W7.1 Puebla-Morelos event close to Mexico City at intermediate depth. First, we discussed the background of intermediate-depth earthquakes (IDEs). Then, we illustrated the earthquake source model and explained how to obtain seismograms in order to compare them to the observed ones. Subsequently, we explored three optimization methods using a benchmark function that has similar properties as the problem of dynamic source inversion, and found that the Particle Swarm Optimization (PSO) method performs best.

Finally, we performed the dynamic source inversion of the Puebla-Morelos earthquake. To this purpose we implemented a PSO algorithm for determining some dynamic parameters of the rupture process following an elliptical source-geometry approximation and a slip-weakening friction law. Our results indicate that rupture was highly dissipative and remarkably slow. More than 84% of the available potential energy for the dynamic rupture propagation dissipated in the focal region. Considering the preexistent slab temperature and heat production associated with the estimated specific fracture energy, creation of pseudotachylytes (friction-induced melts) in the fault-zone is a plausible scenario enhancing rupture propagation. Despite the large dissipation, the source process generated very high accelerations in the fault (i.e. large excitation of short period waves), which contributed to the exceptionally-strong ground motion observed in the epicentral zone and Mexico City. Rupture directivity to the northwest could also have contributed to this observation. Similar and independent estimates of the rupture-energy balance for IDEs in different tectonic settings and geographies strongly suggest that slow, inefficient ruptures with remarkably high energy radiation may represent a preponderant universal feature of earthquakes at intermediate depths.

There are some improvements in the inversion method that could be made. The first is that the problem is at the core a multiobjetive problem. That is, we want to minimize the differences between the observed and synthetic seismograms at various

stations, called misfit. Since the model is very simple, it is not possible to find an optimal function for all stations, and there is a trade-off. Instead of just summing the misfits of all stations and minimize that quantity, it would be more appropriate to apply a multiobjective inversion. Second, it would make the PSO much more powerful if we controlled the density of the population in each model-space region. If there are too many particles in one area, some of them could be redirected to areas which are less explored, giving the method more chances to arrive at the global minimum. Finally, it is desirable to be able to use the knowledge of prior inversions for future ones. At this stage, each inversion starts with no information at all.

We combined information from many fields, but it is important to extend this interdisciplinary approach. The most crucial part is to integrate more information about the petrology. There are many recent laboratory studies that investigate failure mechanisms at conditions under which IDEs occur. With this and the knowledge of the composition of the rocks, we could directly and more convincingly conclude which failure mechanism was operating.

Bibliography

K. Aki and P. G. Richards. *Quantitative seismology*. University Science Books, 2002.

T. B. Andersen, K. Mair, H. Austrheim, Y. Y. Podladchikov, and J. C. Vrijmoed. Stress release in exhumed intermediate and deep earthquakes determined from ultramafic pseudotachylyte. *Geology*, 36(12):995–998, 2008.

L. Astiz, T. Lay, and H. Kanamori. Large intermediate-depth earthquakes and the subduction process. *Physics of the Earth and Planetary interiors*, 53(1-2):80–166, 1988.

I. BoussaïD, J. Lepagnot, and P. Siarry. A survey on optimization metaheuristics. *Information Sciences*, 237:82–117, 2013.

S. Braeck and Y. Podladchikov. Spontaneous thermal runaway as an ultimate failure mechanism of materials. *Physical Review Letters*, 98(9):095504, 2007.

E. K. Burke, G. Kendall, et al. *Search methodologies*. Springer, 2005.

M. Campillo, S. Singh, N. Shapiro, J. Pacheco, and R. Hermann. Crustal structure south of the mexican volcanic belt, base don group velocity dispersion. *Geofísica Internacional*, 35(4), 1996.

M. Clerc. *Particle swarm optimization*, volume 93. John Wiley & Sons, 2010.

M. Cocco, P. Spudich, and E. Tinti. On the mechanical work absorbed on faults during earthquake ruptures. *Earthquakes: radiated energy and the physics of faulting*, pages 237–254, 2006.

O. Coutant. Program of numerical simulation axitra. *Res. Rep. LGIT (in French), Universite Joseph Fourier, Grenoble*, 1989.

V. M. Cruz-Atienza, K. B. Olsen, and L. A. Dalguer. Estimation of the breakdown slip from strong-motion seismograms: Insights from numerical experiments. *Bulletin of the Seismological Society of America*, 99(6):3454–3469, 2009.

V. M. Cruz-Atienza, S. K. Singh, and M. Ordaz. Qué ocurrió el 19 de septiembre de 2017 en méxico? *Revista Digital Universitaria (RDU)*, 18(7), 2017.

L. A. Dalguer and S. M. Day. Staggered-grid split-node method for spontaneous rupture simulation. *Journal of Geophysical Research: Solid Earth*, 112(B2), 2007.

S. Das and B. Kostrov. Inversion for seismic slip rate history and distribution with stabilizing constraints: Application to the 1986 andreanof islands earthquake. *Journal of Geophysical Research: Solid Earth*, 95(B5):6899–6913, 1990.

S. M. Day, L. A. Dalguer, N. Lapusta, and Y. Liu. Comparison of finite difference and boundary integral solutions to three-dimensional spontaneous rupture. *Journal of Geophysical Research: Solid Earth*, 110(B12), 2005.

G. Di Toro, S. Nielsen, and G. Pennacchioni. Earthquake rupture dynamics frozen in exhumed ancient faults. *Nature*, 436(7053):1009, 2005.

J. Díaz-Mojica, V. M. Cruz-Atienza, R. Madariaga, S. K. Singh, J. Tago, and A. Iglesias. Dynamic source inversion of the m6. 5 intermediate-depth zumpango earthquake in central mexico: A parallel genetic algorithm. *Journal of Geophysical Research: Solid Earth*, 119(10):7768–7785, 2014.

D. P. Dobson, P. G. Meredith, and S. A. Boon. Simulation of subduction zone seismicity by dehydration of serpentine. *Science*, 298(5597):1407–1410, 2002.

R. Eberchart and J. Kennedy. Particle swarm optimization. In *IEEE International Conference on Neural Networks, Perth, Australia*, 1995.

S. G. Fattal, E. Simiu, and C. G. Culver. *Observations on the Behavior of Buildings in the Romania Earthquake of March 4, 1977*, volume 490. US Department of Commerce, National Bureau of Standards, 1977.

T. P. Ferrand, N. Hilairet, S. Incel, D. Deldicque, L. Labrousse, J. Gasc, J. Renner, Y. Wang, H. W. Green II, and A. Schubnel. Dehydration-driven stress transfer triggers intermediate-depth earthquakes. *Nature communications*, 8:15247, 2017.

I. Fister Jr, X.-S. Yang, I. Fister, J. Brest, and D. Fister. A brief review of nature-inspired algorithms for optimization. *arXiv preprint arXiv:1307.4186*, 2013.

C. Frohlich. The nature of deep-focus earthquakes. *Annual Review of Earth and Planetary Sciences*, 17(1):227–254, 1989.

C. Frohlich. *Deep earthquakes*. Cambridge university press, 2006.

P. Fulton, E. E. Brodsky, Y. Kano, J. Mori, F. Chester, T. Ishikawa, R. Harris, W. Lin, N. Eguchi, S. Toczko, et al. Low coseismic friction on the tohoku-oki fault determined from temperature measurements. *Science*, 342(6163):1214–1217, 2013.

M. Galis, C. Pelties, J. Kristek, P. Moczo, J.-P. Ampuero, and P. M. Mai. On the initiation of sustained slip-weakening ruptures by localized stresses. *Geophysical Journal International*, 200(2):890–909, 2014.

D. García, S. K. Singh, M. Herráiz, J. F. Pacheco, and M. Ordaz. Inslab earthquakes of central mexico: Q, source spectra, and stress drop. *Bulletin of the Seismological Society of America*, 94(3):789–802, 2004.

H. W. Green and H. Houston. The mechanics of deep earthquakes. *Annual Review of Earth and Planetary Sciences*, 23(1):169–213, 1995.

B. R. Hacker, S. M. Peacock, G. A. Abers, and S. D. Holloway. Subduction factory 2. are intermediate-depth earthquakes in subducting slabs linked to metamorphic dehydration reactions? *Journal of Geophysical Research: Solid Earth*, 108(B1), 2003.

R. Harris, M. Barall, R. Archuleta, E. Dunham, B. Aagaard, J. Ampuero, H. Bhat, V. Cruz-Atienza, L. Dalguer, P. Dawson, et al. The scec/usgs dynamic earthquake rupture code verification exercise. *Seismological Research Letters*, 80(1):119–126, 2009.

J. H. Holland. Adaptation in natural and artificial systems. an introductory analysis with application to biology, control, and artificial intelligence. *Ann Arbor, MI: University of Michigan Press*, pages 439–444, 1975.

Y. Ida. Cohesive force across the tip of a longitudinal-shear crack and griffith's specific surface energy. *Journal of Geophysical Research*, 77(20):3796–3805, 1972.

M. Jamil and X.-S. Yang. A literature survey of benchmark functions for global optimisation problems. *International Journal of Mathematical Modelling and Numerical Optimisation*, 4(2):150–194, 2013.

T. John, S. Medvedev, L. H. Rüpke, T. B. Andersen, Y. Y. Podladchikov, and H. Austrheim. Generation of intermediate-depth earthquakes by self-localizing thermal runaway. *Nature Geoscience*, 2(2):137, 2009.

H. Jung, H. W. Green Ii, and L. F. Dobrzhinetskaya. Intermediate-depth earthquake faulting by dehydration embrittlement with negative volume change. *Nature*, 428 (6982):545, 2004.

H. Kanamori and E. E. Brodsky. The physics of earthquakes. *Reports on Progress in Physics*, 67(8):1429, 2004.

H. Kanamori, D. L. Anderson, and T. H. Heaton. Frictional melting during the rupture of the 1994 bolivian earthquake. *Science*, 279(5352):839–842, 1998.

P. B. Kelemen and G. Hirth. A periodic shear-heating mechanism for intermediate-depth earthquakes in the mantle. *Nature*, 446(7137):787, 2007.

A. Leith and J. Sharpe. Deep-focus earthquakes and their geological significance. *The Journal of Geology*, 44(8):877–917, 1936.

A. Lemoine, R. Madariaga, and J. Campos. Slab-pull and slab-push earthquakes in the mexican, chilean and peruvian subduction zones. *Physics of the Earth and Planetary Interiors*, 132(1-3):157–175, 2002.

R. Madariaga and K. B. Olsen. Criticality of rupture dynamics in 3-d. *Pure and Applied Geophysics*, 157(11-12):1981–2001, 2000.

R. Madariaga, K. Olsen, and R. Archuleta. Modeling dynamic rupture in a 3d earthquake fault model. *Bulletin of the Seismological Society of America*, 88(5): 1182–1197, 1998.

V. C. Manea and M. Manea. Flat-slab thermal structure and evolution beneath central mexico. *Pure and Applied Geophysics*, 168(8-9):1475–1487, 2011.

D. Melgar, X. Pérez-Campos, L. Ramirez-Guzman, Z. Spica, V. H. Espíndola, W. C. Hammond, and E. Cabral-Cano. Bend faulting at the edge of a flat slab: The 2017 mw7. 1 puebla-morelos, mexico earthquake. *Geophysical Research Letters*, 45(6):2633–2641, 2018.

S. Mertens. The easiest hard problem: Number partitioning. *Computational Complexity and Statistical Physics*, 125(2):125–139, 2006.

T. Mikumo, K. B. Olsen, E. Fukuyama, and Y. Yagi. Stress-breakdown time and slip-weakening distance inferred from slip-velocity functions on earthquake faults. *Bulletin of the Seismological Society of America*, 93(1):264–282, 2003.

S. Mirjalili. Sca: a sine cosine algorithm for solving optimization problems. *Knowledge-Based Systems*, 96:120–133, 2016.

Y. Nishitsuji and J. Mori. Source parameters and radiation efficiency for intermediate-depth earthquakes in northeast japan. *Geophysical Journal International*, 196(2):1247–1259, 2013.

K. E. Parsopoulos, M. N. Vrahatis, et al. Particle swarm optimization method for constrained optimization problems. *Intelligent Technologies–Theory and Application: New Trends in Intelligent Technologies*, 76(1):214–220, 2002.

M. Perry, G. A. Spinelli, I. Wada, and J. He. Modeled temperatures and fluid source distributions for the mexican subduction zone: Effects of hydrothermal circulation and implications for plate boundary seismic processes. *Geochemistry, Geophysics, Geosystems*, 17(2):550–570, 2016.

S. E. Persh and H. Houston. Strongly depth-dependent aftershock production in deep earthquakes. *Bulletin of the Seismological Society of America*, 94(5):1808–1816, 2004.

O. Plümper, T. John, Y. Y. Podladchikov, J. C. Vrijmoed, and M. Scambelluri. Fluid escape from subduction zones controlled by channel-forming reactive porosity. *Nature Geoscience*, 10(2):150, 2017.

P. Poli and G. Prieto. Global and along-strike variations of source duration and scaling for intermediate-depth and deep-focus earthquakes. *Geophysical Research Letters*, 41(23):8315–8324, 2014.

P. Poli and G. A. Prieto. Global rupture parameters for deep and intermediate-depth earthquakes. *Journal of Geophysical Research: Solid Earth*, 121(12):8871–8887, 2016.

P. Poli, G. Prieto, E. Rivera, and S. Ruiz. Earthquakes initiation and thermal shear instability in the hindu kush intermediate depth nest. *Geophysical Research Letters*, 43(4):1537–1542, 2016.

R. Poli. Analysis of the publications on the applications of particle swarm optimisation. *Journal of Artificial Evolution and Applications*, 2008, 2008.

G. A. Prieto, G. C. Beroza, S. A. Barrett, G. A. López, and M. Florez. Earthquake nests as natural laboratories for the study of intermediate-depth earthquake mechanics. *Tectonophysics*, 570:42–56, 2012.

G. A. Prieto, M. Florez, S. A. Barrett, G. C. Beroza, P. Pedraza, J. F. Blanco, and E. Poveda. Seismic evidence for thermal runaway during intermediate-depth earthquake rupture. *Geophysical Research Letters*, 40(23):6064–6068, 2013.

G. A. Prieto, B. Froment, C. Yu, P. Poli, and R. Abercrombie. Earthquake rupture below the brittle-ductile transition in continental lithospheric mantle. *Science Advances*, 3(3):e1602642, 2017.

B. Proctor and G. Hirth. Role of pore fluid pressure on transient strength changes and fabric development during serpentine dehydration at mantle conditions: implications for subduction-zone seismicity. *Earth and Planetary Science Letters*, 421:1–12, 2015.

C. B. Raleigh and M. Paterson. Experimental deformation of serpentinite and its tectonic implications. *Journal of Geophysical Research*, 70(16):3965–3985, 1965.

C. R. Ranero, A. Villaseñor, J. Phipps Morgan, and W. Weinrebe. Relationship between bend-faulting at trenches and intermediate-depth seismicity. *Geochemistry, Geophysics, Geosystems*, 6(12), 2005.

S. Ruiz and R. Madariaga. Kinematic and dynamic inversion of the 2008 northern iwate earthquake. *Bulletin of the Seismological Society of America*, 103(2A):694–708, 2013.

M. Scambelluri, G. Pennacchioni, M. Gilio, M. Bestmann, O. Plümper, and F. Nestola. Fossil intermediate-depth earthquakes in subducting slabs linked to differential stress release. *Nature Geoscience*, 10(12):960, 2017.

Y. Shi and R. Eberhart. A modified particle swarm optimizer. In *Evolutionary Computation Proceedings, 1998. IEEE World Congress on Computational Intelligence., The 1998 IEEE International Conference on*, pages 69–73. IEEE, 1998a.

Y. Shi and R. C. Eberhart. Parameter selection in particle swarm optimization. In *International conference on evolutionary programming*, pages 591–600. Springer, 1998b.

S. Singh, E. Reinoso, D. Arroyo, M. Ordaz, V. Cruz-Atienza, X. Pérez-Campos, A. Iglesias, and V. Hjörleifsdóttir. Deadly intraslab mexico earthquake of 19 september 2017 (mw7.1): Ground motions and damage pattern in mexico city. *Under review in Bull. Seismic. Soc. Am.*, 2018.

S. K. Singh, M. Ordaz, X. Pérez-Campos, and A. Iglesias. Intraslab versus interplate earthquakes as recorded in mexico city: Implications for seismic hazard. *Earthquake Spectra*, 31(2):795–812, 2015.

S. Stein and M. Wysession. *An Introduction to Seismology, Earthquakes, and Earth Structure*. Blackwell publishing, 2003.

R. Storn and K. Price. Differential evolution–a simple and efficient heuristic for global optimization over continuous spaces. *Journal of global optimization*, 11(4): 341–359, 1997.

P. N. Suganthan. Particle swarm optimiser with neighbourhood operator. In *Evolutionary Computation, 1999. CEC 99. Proceedings of the 1999 Congress on*, volume 3, pages 1958–1962. IEEE, 1999.

M. Suzuki and Y. Yagi. Depth dependence of rupture velocity in deep earthquakes. *Geophysical Research Letters*, 38(5), 2011.

A. Torn and A. Zilinskas. *Global optimization*. Springer-Verlag New York, Inc., 1989.

M. Vallée. Source time function properties indicate a strain drop independent of earthquake depth and magnitude. *Nature communications*, 4:2606, 2013.

F. Van den Bergh and A. P. Engelbrecht. A cooperative approach to particle swarm optimization. *IEEE transactions on evolutionary computation*, 8(3):225–239, 2004.

A. Venkataraman and H. Kanamori. Observational constraints on the fracture energy of subduction zone earthquakes. *Journal of Geophysical Research: Solid Earth*, 109(B5), 2004.

K. Wadati. Unusual nature of deep-sea earthquakes—on the three types of earthquakes. *Kishoshushi*, 6:1–43, 1928.

D. A. Wiens. Seismological constraints on the mechanism of deep earthquakes: Temperature dependence of deep earthquake source properties. *Physics of the Earth and Planetary Interiors*, 127(1-4):145–163, 2001.

X.-S. Yang. *Nature-inspired metaheuristic algorithms*. Luniver press, 2010.

X.-S. Yang. *Nature-inspired optimization algorithms*. Elsevier, 2014.

List of Figures

Appendices

The September 19th, 2017 (M_W7.1), intermediate-depth Mexican earthquake: a slow and energetically inefficient deadly shock

Aron Y.S. Mirwald[1], Víctor M. Cruz-Atienza[1], John Díaz-Mojica[1], Arturo Iglesias[1], Shri K. Singh[1], Carlos Villafuerte[1], and Vala Hjörleifsdóttir[1]

[1]Department of Seismology, National Autonomous University of Mexico, Mexico City

Preliminary manuscript for submission in the Geophysical Research Letters

Abstract

Although intermediate-depth earthquakes (IDE) pose a serious seismic hazard, the physics of their source process is still under debate. We invert dynamic rupture parameters of the M_W7.1 Puebla-Morelos IDE (h = 57 km), which caused a devastation in Mexico City. Our simple, elliptical source model coupled with a new Particle Swarm Optimization algorithm reveals that rupture propagated to the north-west within the subducted Cocos plate, showing a high stress drop ($\Delta\tau = 14.2 \pm 5.8$ MPa) and a remarkably low radiation efficiency ($\eta_r = 0.16 \pm 0.09$). Fracture energy is large ($G = (1.0 \pm 0.3) \times 10^{16}$ J), producing a slow dissipative rupture ($V_r/V_s = 0.34 \pm 0.04$) with scaling-consistent radiated energy ($E_r = (1.8 \pm 0.9) \cdot 10^{15}$ J) and energy-moment ratio ($E_r/M_0 = 3.2 \times 10^5$). About 84% of the available potential energy for the dynamic rupture was deposited in a compact focal region, strongly suggesting a large heat production and possibly fault-core melting. Such earthquake features seem to be a universal signature of IDEs.

1 Introduction

Mexico City is highly vulnerable to earthquakes due to the large amplification of seismic waves caused by the lakebed sediments on which a large part of the city is built. The greatest damage ever suffered in the city has been produced by a thrust event (1985 Michoacán, M_W8.0), with over ten thousand deaths. Although less frequent and generally smaller, intermediate-depth earthquakes may also produce large damages in Mexico City and other urban areas in Central Mexico because of their proximity and large radiation of high frequencies (*García et al.*, 2004). Actually, the exceedance rate of Peak Ground Acceleration (PGA) in the city from both thrust, interplate and normal, intermediate-depth (intraslab) events is about the same (*Singh et al.*, 2015).

On September 19th 2017, an M_W7.1 intermediate-depth earthquake (IDE) took place below the border of Puebla and Morelos states in the subducting Cocos plate at 57 km depth, with epicentral distance of 114 km from Mexico City (*Singh et al.*, 2018) (Figure 1). The peak ground acceleration at the hard-rock reference site of Ciudad Universitaria (CU) was 57 gal, twice the largest ever recorded of 29 gal due to the 1985 earthquake (*Cruz-Atienza et al.*, 2017). 369 people died in Mexico, from which 228 perished in the capital where 43 buildings collapsed. Such devastation produced by an IDE is not exceptional. Several past intraslab earthquakes in Mexico, as the great M_W8.2 rupture offshore the states of Oaxaca and Chiapas in September 8th, 2017 (*Okuwaki and Yagi*, 2017; *Suárez et al.*, 2018), have also caused large damage in other regions of the country (see *Singh et al.* (2018) for a historical overview of IDEs in Mexico).

Despite the hazard that IDEs represent in Mexico and other regions of the globe, the physics of this kind of earthquakes has challenged the seismological community for decades (*Frohlich*, 2006). At focal depths

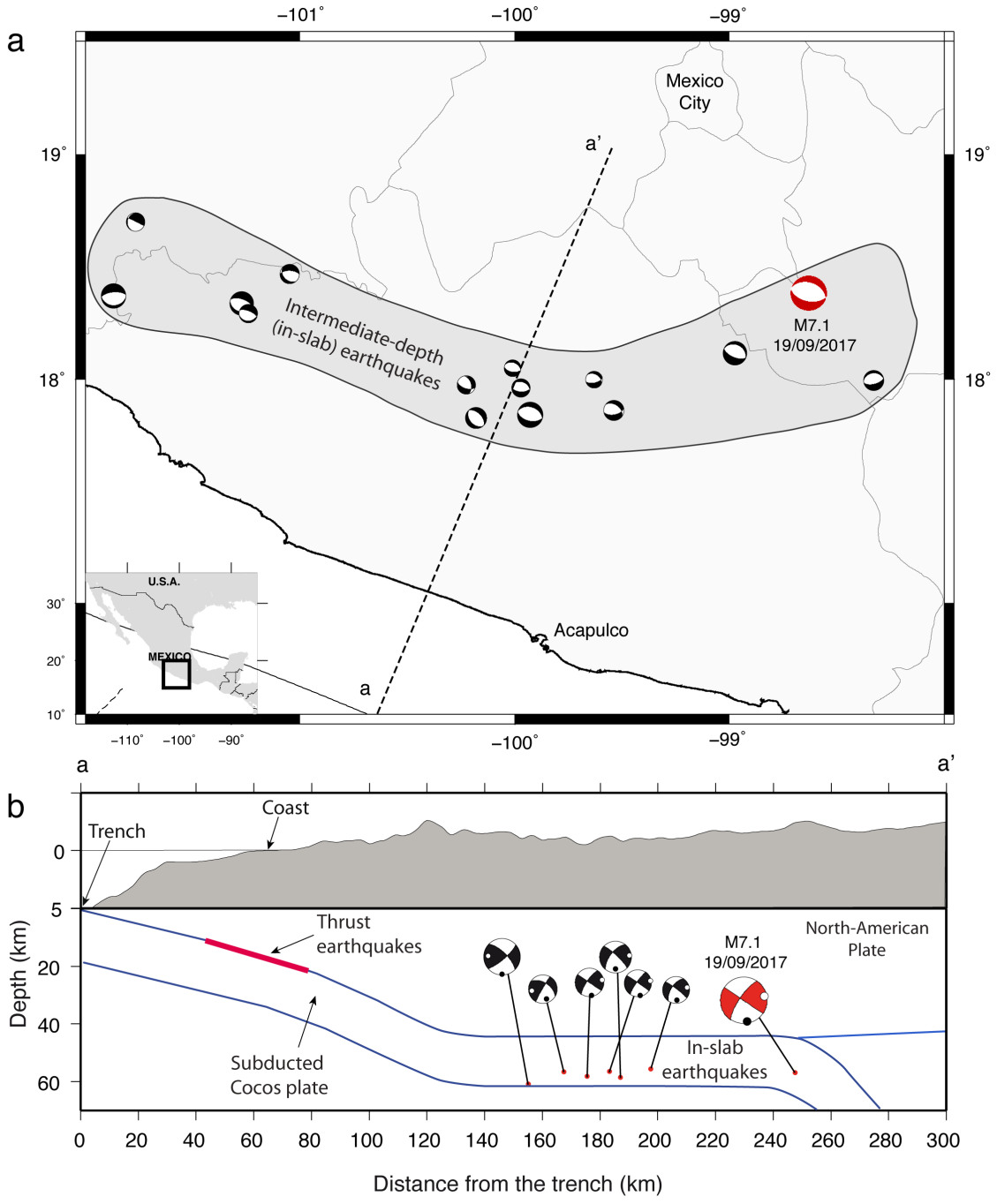

Figure 1: Locations of Mexican IDEs. The red beach ball represents the Puebla-Morelos event (after *Cruz-Atienza et al.* (2017)

below 30 kilometers, brittle failure should be inhibited due to the high normal stresses and frictional stability (*Scholz*, 1998; *Green and Houston*, 1995). Yet most IDEs are characterized by unstable slip radiating high frequencies (*Frohlich*, 2006). Dehydration reactions at those depths have often been invoked to explain brittle fracture based on the spatial correlation between IDEs and water-rich mineralogical phases in the subducted slab (*Hacker et al.*, 2003). Water release from phase transitions counteracts the confining pressure, lowering the effective pressure and enabling brittle fracture (*Prieto et al.*, 2012). Dehydration driven stress-transfer (*Ferrand et al.*, 2017) may also contribute to such instabilities provided that volume changes due to the phase transition is negative, a likely condition at depths below 60 km (*Jung et al.*, 2004). Differential stresses produced by the slab unbending seems also a plausible mechanism triggering IDEs (*Scambelluri et al.*, 2017).

However, it is possible that brittle fracture is not at all responsible for IDEs. Thermal runaway in the focal region is a likely candidate generating highly localized ductile deformation and slip instabilities (*Kanamori et al.*, 1998; *Prieto et al.*, 2012). This mechanism was shown to be viable by numerical computations (*Braeck and Podladchikov*, 2007; *John et al.*, 2009). Geological evidence also supports this mechanism (*John et al.*, 2009; *Andersen et al.*, 2008). One advantage thermal runaway has over dehydration embrittlement is that it could explain the occurrence of IDEs in absence of dehydration, as the 2013 Wyoming earthquake (*Prieto et al.*, 2017). Recent seismological studies suggest that thermal shear runaway is the leading rupture mechanism in the focal region of IDEs (*Prieto et al.*, 2013, 2017).

Recent advances in source imaging allow the determination of some dynamic rupture parameters directly from ground motion records. After the pioneer work of *Peyrat and Olsen* (2004), where they performed a dynamic source inversion of the Tottori (2000) earthquake, a few other efforts have led to improved methodologies for inverting the friction and stress changes on seismogenic faults (*Di Carli et al.*, 2010; *Ruiz and Madariaga*, 2013; *Díaz-Mojica et al.*, 2014; *Twardzik et al.*, 2014; *Herrera et al.*, 2017). Since these methods model the spontaneous rupture process to explain the observed seismograms (by solving the elastodynamic equations for wave propagation coupled with a fault-friction constitutive law), they allow assessing fundamental properties of the source such as the energy partition and its relation with the rupture kinematics. In this sense, the dynamic source inversion represents a powerful alternative to elucidate more about the physics of IDEs.

On December 11th of 2011 an M_W6.5 IDE took place close to Zumpango, Mexico, about 140 km southwest of the 2017 (M_W7.1) Puebla-Morelos event. With similar depth and focal mechanism, both earthquakes are the consequence of trench-perpendicular tensional stresses in the oceanic lithosphere below the continent. *Díaz-Mojica et al.* (2014) performed the dynamic source inversion of the earthquake providing unexpected conclusions for a highly intense event. With a typical stress drop for IDEs in Mexico of 29.2 ± 6.2 MPa (*García et al.*, 2004), both the average rupture velocity ($v_r/v_s = 0.47 \pm 0.09$) and the radiation efficiency ($\eta_r = 0.26 \pm 0.1$) were remarkably low. Although the energy-moment ratio ($E_r/M_0 = 5.7 \cdot 10^5$) was similar to most shallow earthquakes (*Kanamori and Brodsky*, 2004), the fracture energy was almost three times larger than the radiated energy.

Remarkably, these conclusions point in the same direction as those of a contemporary and independent investigation in the Japan subduction zone (*Nishijutsu and Mori*, 2013), where the empirical analysis of 216 IDEs also revealed that this kind of earthquakes have radiation efficiencies lower than shallow ruptures, suggesting a preponderant source-dissipative mechanism at intermediate depths. The recent analysis of an M_W4.8 IDE in a completely different tectonic setting, far from any convergent plate boundary, revealed a very similar rupture process (*Prieto et al.*, 2017). This event, which took place in the lithospheric mantle of Wyoming, USA, share the same source dynamics determined for the 2011 intraslab Mexican earthquake: high stress drop, low rupture velocity and low radiation efficiency, suggesting a possibly universal energy partition mechanism for IDEs.

In this work, we present the dynamic source inversion of the Puebla-Morelos (2017) earthquake to in-

Table 1: P- and S-Velocities from *Campillo et al.* (1996).

Depth (km)	v_s (m/s)	v_p(m/s)	ρ (km/m^3)
0-5	3100	5370	2490
5-17	3300	5720	2600
17-45	3800	6580	2880
> 45	4700	8140	3380

vestigate the physics of the source process that originated the devastating ground motion in Mexico City. To this purpose, we improved the methodology introduced by *Díaz-Mojica et al.* (2014) by implementing a new Particle Swarm Optimization algorithm (*Eberhart and Kennedy*, 1995) that takes advantage of parallel computing and allows a statistical analysis of the solution.

2 Dynamic Source Inversion

2.1 Source Model

We model the earthquake rupture as a frictional process on a fault plane embedded in a 3-D elastic full space. Sliding begins when the shear traction in the nucleation zone (NZ) exceeds the static fault strength. In nature, the traction builds up gradually due to tectonic loading. Here, the traction in the NZ, that we assume as a 3 km-radius circular patch, is prescribed slightly higher than the static strength of the fault so that the spontaneous rupture initiates with the simulation. To stop the rupture propagation, we assume a barrier model that makes the strength of the rock very high outside the source. To minimize the number of the inversion parameters, the rupture area has an elliptical shape, which is a reasonable constraint for moderate size IDEs that generally show simpler and localized slip distributions. The geometry of the source model is thus determined by 5 parameters that are the length of the two semi axis, the two coordinates in the fault plane of the center of the ellipse with respect to the NZ, and the rotation angle of the ellipse on the fault plane.

We adopt the linear slip-weakening friction law (*Ida*, 1972), which captures key features of earthquakes and only depends on three constitutive parameters: the static (μ_s) and dynamic (μ_d) friction coefficients, and the slip weakening distance (D_c). We assumed a constant fault normal traction equal to the lithostatic pressure at 60 km depth (1564 MPa), although this is irrelevant for the rupture process because seismic radiation only depends on the relative stress changes. We fixed μ_d equal to 0.5 and inverted for the change of friction coefficient from the static to the dynamic levels, $\Delta\mu$.

Altogether, the source model is determined by nine parameters: the initial shear traction in the NZ, the initial shear traction outside the NZ, the change of the friction coefficient, the slip weakening distance, and the five geometrical parameters of the ellipse. From models parameterized in such a way, we can derive physical quantities involved in the energy partition of the rupture process (*Díaz-Mojica et al.*, 2014) such as the fracture energy, G, the radiated energy, E_r, and the radiation efficiency, $\eta_r = E_r/(E_r + G)$, which tells how dissipative is the rupture process.

2.2 Inversion Method

The dynamic rupture problem is highly nonlinear and multiparametric so linearized inversion methods are inappropriate to find the global minimum of the optimization problem. It is neither possible to perform an exhaustive grid search of the model space due to the highly expensive computational cost of the forward problem as described later. For these reasons, the dynamic source inversion problem has been solved using heuristic strategies such as the neighborhood (e.g. *Di Carli et al.* (2010); *Ruiz and Madariaga* (2013)) and

genetic algorithms (*Díaz-Mojica et al.*, 2014). In this work we introduce a new strategy to solve the problem aiming to its remarkable capacity to guide the search in the model space by sampling exhaustively the neighborhood of the optimal solution, which makes possible a statistical analysis of the selected models. This is the Particle Swarm Optimization (PSO) algorithm, which has proven to be very efficient for a large class of problems (*Blum and Li*, 2008). We implemented the same PSO algorithm as *Suganthan et al.* (1999), the only difference being the size of the neighborhood, which changes between 5 and 50% of the whole population (instead of 60-100%). The size of the population was 420 models, and we ran the inversions for 50 generations, resulting in a total of 21000 calculated models. In table 2 we provide the searching range of the inversions for each parameter. To avoid wasting computational time with infeasible models, we constrained the parameters in such way that the initial traction was always larger and lower than the static strength of the rock in the NZ and the rest of the fault-plane, respectively.

To quantify the quality of the source models we use a misfit function that involves the cross-correlation between observed and synthetic seismograms (*Díaz-Mojica et al.*, 2014):

$$f = \sum \left(\frac{\tau_{max} + \tau_c}{2\tau_c} - \frac{\text{cross}(x_{obs} - x_{syn}}{\text{auto}(x_{obs}) + \text{auto}(x_{syn})} \right), \tag{1}$$

where the sum is over the three components of all seismic stations. The second term on the right-hand side is the maximum of the cross-correlation, and accounts for the similarity of waveform and amplitude. The first term accounts for the time shift between the signals, which is scaled with the characteristic time, τ_c, approximately equal to the source-duration halftime.

Following *Di Carli et al.* (2010), to compute the synthetic waveforms involved in Equation 1, the method solves the forward problem in two steps. First the dynamic rupture simulation is performed, and second the output source kinematics is used to propagate the wave-field up to the stations. The dynamic rupture is simulated using a highly efficient 3D traction-at-slip-node finite-difference method (*Dalguer and Day*, 2007) in a cubic domain where the fault is embedded, with 50 km edge lengths and a grid size of 400 m. We verified that such a grid size produces virtually the same solutions as with 300 m, which is an expected result to guarantee the numerical convergence of this method (*Dalguer and Day*, 2007). The time step was adjusted according to the stability limit. The cube contains the fault-plane on which the friction law operates. Around the cube, the outgoing seismic energy is absorbed with a Perfectly Matched Layer (*Marcinkovich and Olsen*, 2003) to simulate an infinite space. Following *Díaz-Mojica et al.* (2014), the propagation of the wave-field from the source to the stations is carried out by convolving the slip-rate function with double-couple Green's functions computed with a discrete wave-number method (*Bouchon*, 1981) in a layered medium appropriate for the region shown in Table 1 (*Campillo et al.*, 1996).

2.3 Data and Focal Mechanism

The inversion was performed using accelerograms of 6 strong motion stations belonging to the National University of Mexico (UNAM) with an epicentral distance smaller than 110 km (see Figure 2). We selected the stations avoiding those with large site-effects, while maintaining a good azimuthal coverage (Figure 1). We first aligned the seismograms with the theoretical P-wave arrivals predicted by the regional velocity model of Table 1. The accelerograms were bandpass filtered between 0.05 and 0.15 Hz and integrated twice to obtain the displacements that were inverted. The corner frequency of the event is ∼0.08 Hz, which is consistent with the source time function duration of ∼13 s reported by the USGS. The inverted frequency band thus includes essential information of the source finiteness. We choose the upper cutoff frequency because of the simplicity of both the source model and the 1D velocity structure, that prevent us to solve for rupture details that are actually irrelevant for capturing the overall physics of the source.

Since it was not possible to determine the fault plane unambiguously using the aftershocks sequence, we inverted the source process for both auxiliary planes (Figure 1). The inversion yielded similar model

parameters for both planes, so we decided to discuss only the results for the fault mechanism dipping to the south ($\phi = 108°$, $\delta = 47°$, $\lambda = 98°$), which yielded 20% better fits with the observed waveforms.

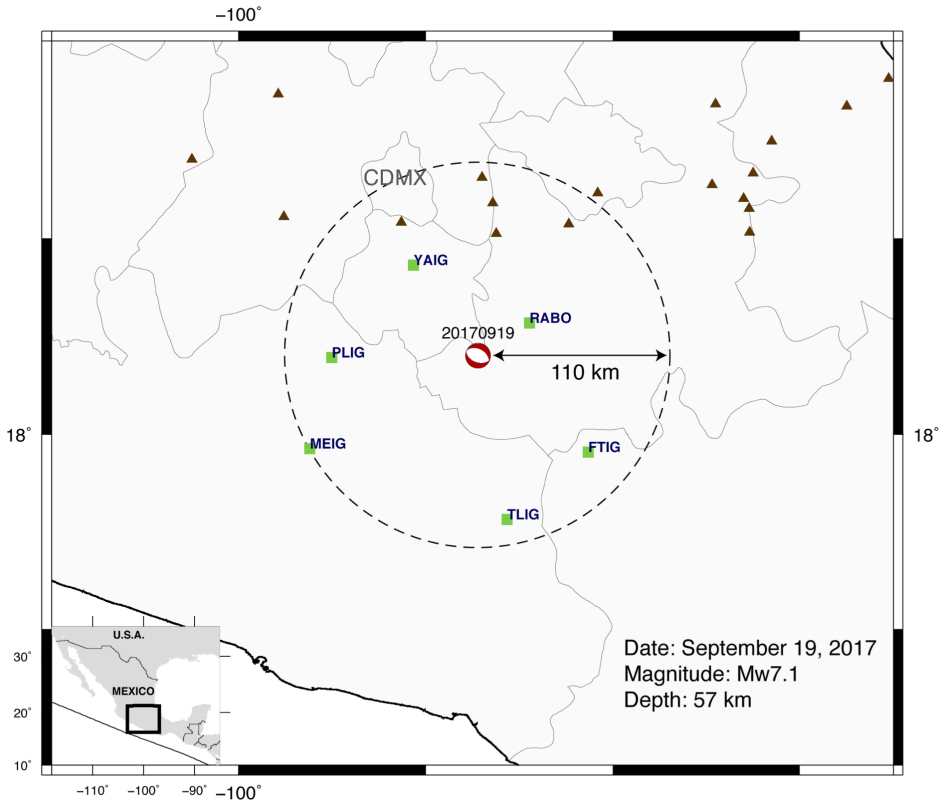

Figure 2: Location and focal mechanism of the Puebla-Morelos event (red beachball) along with the six strong motion stations that were used for the inversion. Brown triangles represent main volcanoes.

3 Results

Due to the stochastic nature of the optimization method, we decided to run multiple inversions. Although misfit values from all inversions were of the same order, we noticed that parameters from the preferred models were different to some extend and that they are physically interdependent. As expected, larger stress-drop is generally accompanied by smaller area and larger D_c, or lower rupture velocity with larger D_c. *Ruiz and Madariaga* (2013) noticed similar trade-offs between the parameters for similar dynamic source inversions. However, the variation range of the preferred model parameters from our inversions are relatively small. Even more importantly, there are invariant physical parameters across the models such as the radiated energy, fracture energy, radiation efficiency, rupture velocity and rupture area. This means that, for explaining the data, all solution models share the same energy partition and rupture kinematics.

The selected models correspond to the best-fit solutions from 12 independent inversions whose misfit values are smaller than 0.15. The final solution (Table 2) is thus the average of these models along with their standard deviation. If the time-shift (τ_c) between the signals was zero, our misfit threshold of 0.15 implies that the second term on the right-hand side of Equation 1, which is known as the semblance, is smaller

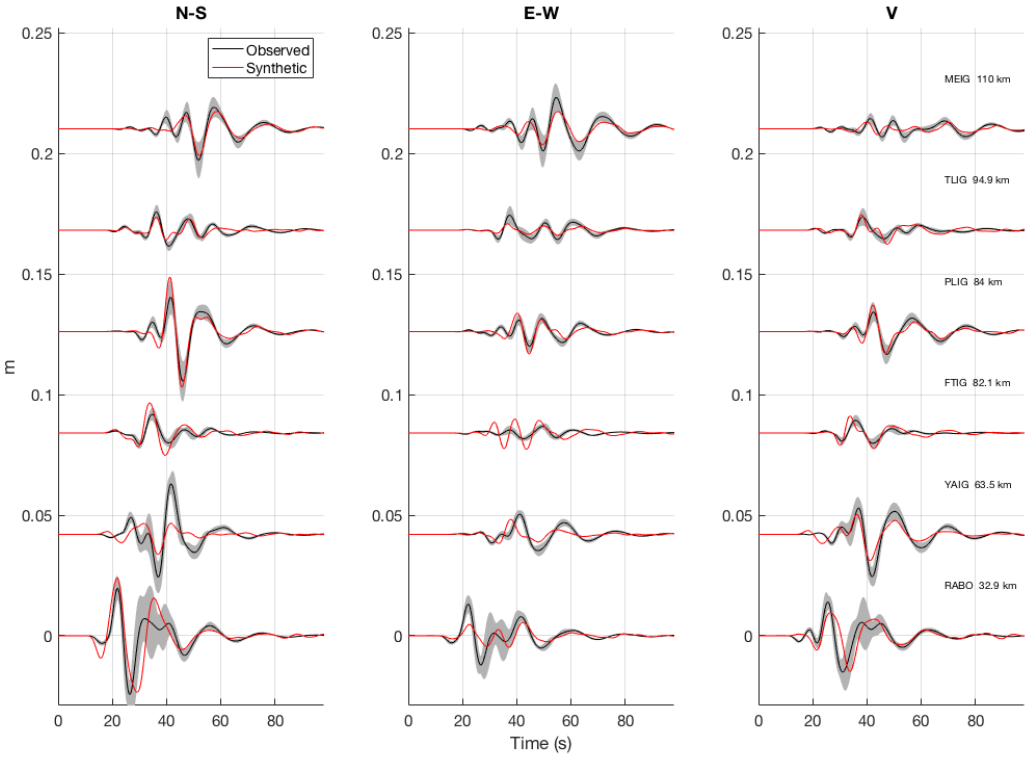

Figure 3: Observed and inverted seismograms. The black line is the average of all inversions, and the grey area is two times the standard deviation.

than 0.35. In this sense, since 0.5 is its highest possible value, our selected models explain more than about 70% of the observed waveforms. The seismograms fits are shown in Figure 3, where we compare the average waveforms from the selected models (black curves) along with the associated standard deviations (gray band). Despite the simplicity of the source model and the velocity structure, most of the main waveform characteristics are well reproduced, which gives confidence to our model solutions.

In Figure 4a we show the average final slip from the 12 selected models and the geometry of the best-fit solution whose misfit value is 0.11 (white dashed ellipse). Rupture predominantly propagates to the northwest an updip with an average final slip of 2.1 ± 0.3 m, which is a reasonable value for earthquakes of this size. If we project the rupture path from the NZ to the rupture left extremity into the Earth's surface, rupture directivity points roughly towards Mexico City. This could partly explain the anomalously high accelerations observed in that direction (*Singh et al.*, 2018). It is worth mentioning that a consistent direction of rupture directivity was found for all solutions obtained from the inversions in the other auxiliary fault plane, dipping to the north (not shown).

Although rupture velocity is remarkably low across large parts of the fault (average speed of 0.34 ± 0.04 of the shear wave speed (see Table 2)), it is also highly variable (Figure 4b). Just after nucleation, rupture reaches velocities around $0.5V_s$ along $\sim$10 km updip from the NZ and then slows down rapidly, specially

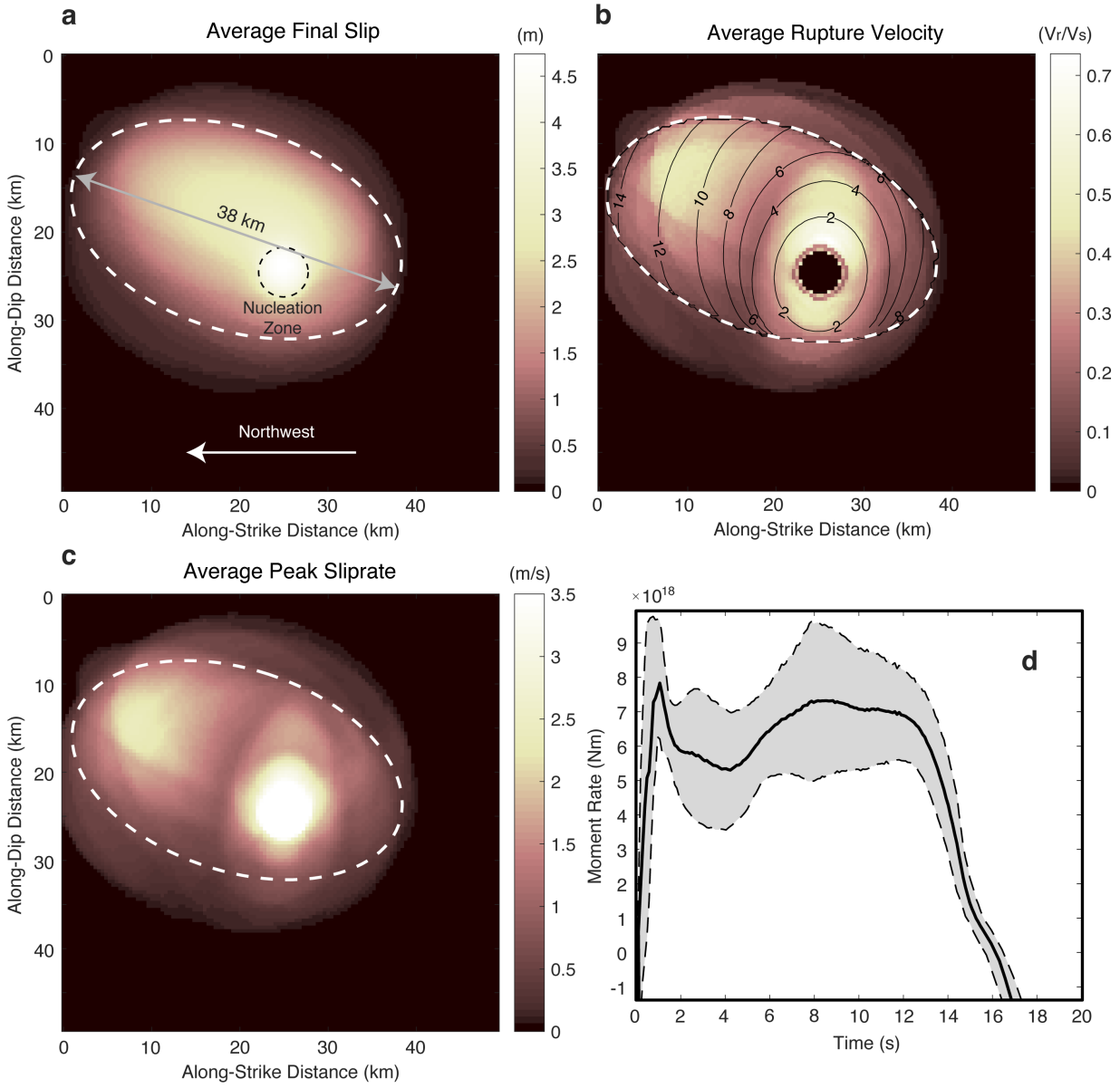

Figure 4: Average final slip (a), average rupture velocity normalized by the shear wave speed of 4.7 km/s along with the rupture time contours of the best-fit model (b), average peak sliprate (c) and the average moment rate function along with the standard deviation in gray (d). The dashed white ellipse depicts the geometry of the best fitting model. All models share the same nucleation zone geometry (black dashed circle).

along-strike, where it almost stops a few kilometers to the northwest. Rupture finally accelerates around 20 km from the NZ to reach values around $0.5V_s$ close to the northwest fault extremity.

Cracks theory predicts that the faster the rupture front, the larger is the radiation efficiency. This is shown in Figure 5 for the three different faulting modes (gray lines). Since fracture energy is almost constant across the fault because of our friction model, rupture speed variations should map bulk regions where radiation of seismic energy (or the seismic-moment rate) is enhanced. Figure 4c confirms such prediction by revealing two maximum of the peak slip-rate that spatially correlate with fault regions where V_r is maximum (compare with panel b). Consistently, the average moment rate function (Figure 4d) shows two bumps centered at 1 and 10 s, as well as a total source duration close to 16 s. We notice that the first peak is somehow an artifact due to the initial kick in the dynamic rupture nucleation .

The inversion yielded a stress drop of 14.9 ± 5.6 MPa, which is high compared with typical values for shallow earthquakes, but expected for IDEs in Mexico (*García et al.*, 2004) and at a global scale with mean value of ∼15 MPa (*Prieto et al.*, 2012; *Poli and Prieto*, 2016). From the inverted parameters, we derived a radiated energy $E_r = (1.8 \pm 0.9) \cdot 10^{15}$ J, a fracture energy $G = (1.04 \pm 0.3) \cdot 10^{16}$ J and a remarkably low radiation efficiency $\eta_r = 0.16 \pm 0.09$. All the inverted and derived parameters from the inversions are reported in Table 2.

As compared with the magnitude M_w7.1 determined by the Mexican Servicio Sismológico Nacional (SSN) using the regional W-phase, all inversion we carried out yielded a magnitude overestimation with a mean value of $M_w 7.28 \pm 0.07$. This is likely due to lack of low frequencies below 0.05 Hz because of the bandpass filtering required for the double integration of accelerograms. We obtained the similar overestimation for synthetic inversion tests in the same frequency band, but recovered a stress drop and other derived parameters very close to the target values, so we are confident of our energy partition estimates for the actual M_w7.1 earthquake.

4 Discussion

In agreement with the analysis of the 2001 Zumpango IDE (M_w6.5) in Guerrero, Mexico (*Díaz-Mojica et al.*, 2014), the inversion of the Puebla-Morelos event revealed that the rupture speed ($v_r/v_s \sim 0.34$) and the radiation efficiency (η_r ∼0.16) are remarkably low (Figure 5). Besides, as expected for most intraslab Mexican earthquakes, the stress drop ($\Delta\tau$ ∼14 MPa) is relatively high. Similar results for IDEs were found in the Japan subduction zone (*Nishijutsu and Mori*, 2013), and more recently at a global scale (*Poli and Prieto*, 2016) and below the Wyoming Craton, USA, in a completely different tectonic setting (*Prieto et al.*, 2017), suggesting that slow, inefficient source processes may predominantly characterize the rupture process of IDEs.

Although such rupture properties are typical of tsunami earthquakes (see Figure 5), the 2017 M_w7.1 shock produced Fourier accelerations two times larger than observed between 1 and 2 s for Mexican IDEs with similar magnitude reduced to the same hypocentral distance (*Singh et al.*, 2018). This means that despite the highly dissipative and slow source process, the event produced high radiation of short period waves, which is opposite to tsunami earthquakes characterized by large $M_S - M_W$ disparities. It is possible that rupture directivity contributed to this observation. However, our dynamic source model could also explain the strong shaking without rupture directivity. Considering the slip-weakening distance of 0.6 m (Table 2) and taking $\dot{D} = 2.0$ m/s as the mean slip-rate within the two highly-radiative fault regions shown in Figure 4c, the stress breakdown should have taken place in about 0.3 s. Since the peak slip rate (PSR) is approximately reached at the time when the stress drop is completed (*Mikumo et al.*, 2003; *Cruz-Atienza et al.*, 2009), then considering the maximum PSR values in both regions between 2.5 and 3.5 m/s, the focal particles acceleration (i.e. the peak fault accelerations) during the stress drop (i.e. at the slip onset on every fault point) should be significantly higher than 0.5g, that is between 415 and 585 *gal*. These values are consistent with observations at RABO, the closest station (hypocentral distance of 65 km), where the

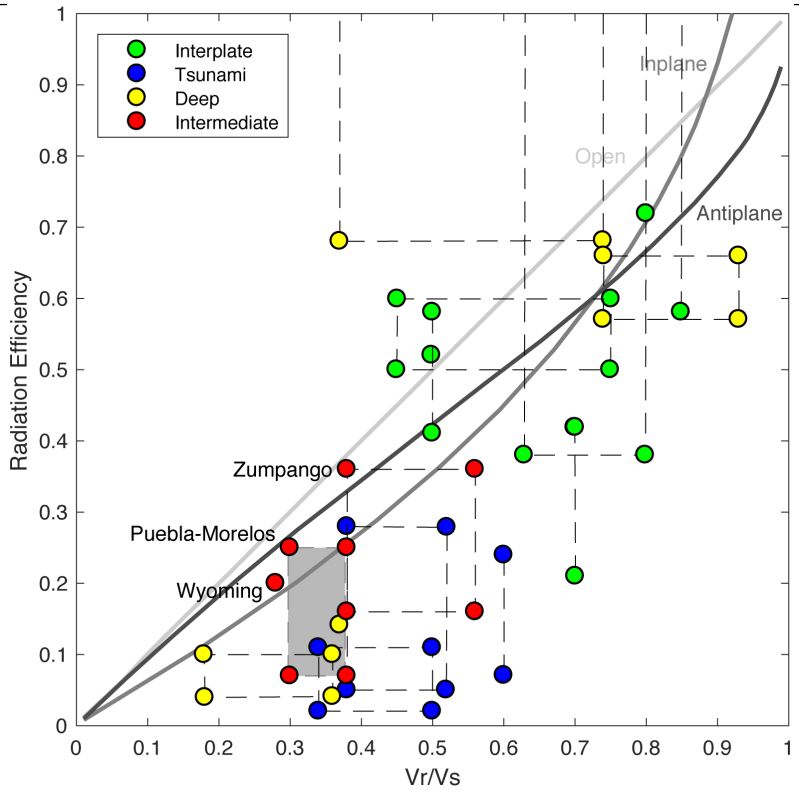

Figure 5: Radiation efficiency (η_r) as a function of rupture velocity (Vr) normalized by the shear wave speed (Vs) for different types of earthquakes including the Puebla-Morelos event. Reported IDEs (red dots) share the same properties as tsunami earthquakes, with very low average rupture velocity and radiation efficiency. Gray lines depict theoretical predictions for the three different deformation modes. Modified from *Kanamori and Brodsky* (2004).

observed Peak Ground Acceleration was 153 *gal*.

Most interplate earthquakes have radiation efficiencies larger than 0.5 (*Venkataraman and Kanamori*, 2004) (Figure 5), which implies $G < E_r$. Since $\eta_r \sim 0.16$ for the Puebla-Morelos event, then $G = 5.8E_r$ in this case. This implies that ∼84% of the available potential energy for the dynamic process of faulting was not radiated, which means that a large amount of energy was dissipated in the focal region. Does fault-zone melting could happen due to heat production? At the very tip of the rupture (i.e. in the stress breakdown zone), the temperature rise (ΔT) is related to the specific fracture energy (G_c) as (*Prieto et al.*, 2013)

$$\Delta T = \frac{G_c}{C\rho w}, \tag{2}$$

where $C \sim 1$ J/g°C is the heat capacity, ρ ∼3230 kg/m^3 and w is the fault-zone width. This equation assumes that the whole fracture energy is dissipated as heat, which is a reasonable first-order approximation considering that over 90% of the fracture energy is converted into heat (*Cocco et al.*, 2006). In our model, G_c (or breakdown work density, namely $W_b = G/A$) is equal to $(1.7 \pm 0.9) \cdot 10^7$ J/m^2 in average. In Figure 6 we show the temperature change for different fault widths predicted by Equation 2. According to thermal models of the subducted Cocos plate (*Manea and Manea*, 2011; *Perry et al.*, 2016), the temperature of the slab where the earthquake took place is between $600 - 700$°C. The melting temperature

of peridotite at those depths range between 1400° and 1800°C (*Prieto et al.*, 2013). Therefore, we expect melting to occur at fault widths between 0,2-1.2 cm (see figure 6). Field observations show that fault width is highly variable, but most fault veins are between 0.1-3 cm(*Prieto et al.*, 2013). Therefore, the temperature rise at the rupture front may have indeed resulted in rock melting as suggested for other IDEs (*Prieto et al.*, 2013). Note that we did not include the total heat generated during the slip as *Kanamori et al.* (1998).

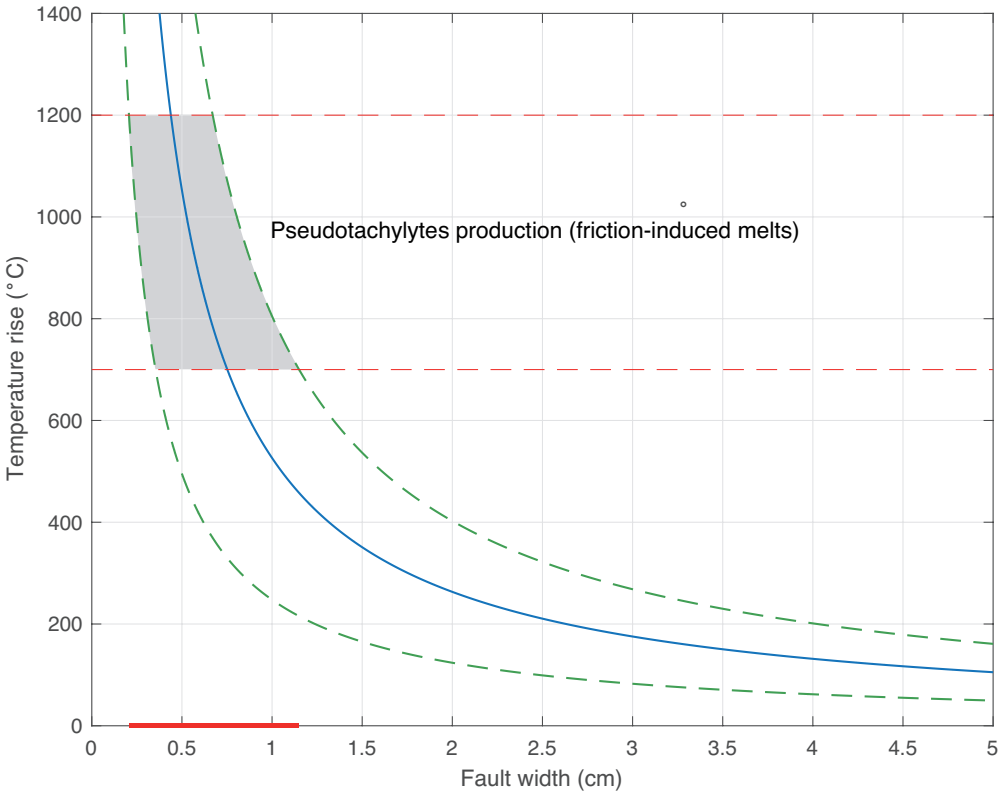

Figure 6: Temperature difference according to Equation 2.

The slow rupture velocity and low radiation efficiency of the Puebla-Morelos event (Figure 5) indicate that the rupture was highly dissipative. Rupture dissipation may involve different processes such as off-fault fracturing or plastic deformation. However, heat production is certainly one of the most prominent dissipative mechanisms that translate into pseudotachylytes production (friction-induced melts) in the fault-core (*Di Toro et al.*, 2005) or heat flux (*Fulton et al.*, 2013). Our heat production estimate suggests that melting may have already occurred at the rupture tip, consistent with thermal runaway as the main physical mechanism driving the rupture process, as proposed by previous authors for IDEs in the Bucaramanga Nest (*Prieto et al.*, 2013). Dehydration from water-rich minerals could also have played a complementary role in the source process, which doesn't preclude the thermal runaway mechanism (*John et al.*, 2009).

The hypocenter of the Puebla-Morelos event is located close to the slab segment where the subducted plate bends to sink down into the mantle (Figure 1b). Unlike a previous kinematic source imaging of the event (*Melgar et al.*, 2018), our preferred rupture model indicates that the active fault dips southward and

Table 2: Inversion model-parameters ranges, and inverted and derived values.

		Range	Inverted
D_c	Slip-weakening distance	0.2-1 m	0.6 ± 0.3 m
A	Area	$80 - 1250$ km^2	713 ± 250 km^2
$\Delta\tau$	Stress-drop	0-48 MPa	14.9 ± 5.6 MPa
$\Delta\tau^n$	Stress-drop in NZ	18-78 MPa	55 ± 11 MPa
$\Delta\mu$	Difference of friction parameter	0.015 - 0.5	0.035 ± 0.007
G	Fracture energy	-	$(1.04 \pm 0.3) \cdot 10^{16}$J
E_r	Radiated energy	-	$(1.8 \pm 0.9) \cdot 10^{15}$J
κ	$\sim$ ratio of strain energy to G_c	-	1.5 ± 0.2
η_r	Radiation efficiency	-	0.16 ± 0.09
V_r	Rupture velocity	-	$(0.34 \pm 0.04)v_s$
M_w	Moment Magnitude	-	7.28 ± 0.07

that rupture propagated along-strike and updip. Such rupture process make sense considering that (1) preexistent plate-interface perpendicular fractures in the slab reorient with such dipping angle as the plate bends down, and (2) flexural stresses produce a reduction of the fault-normal traction (i.e. of the fault strength) towards the surface. The second argument may explain why rupture initiated in a deep focal region and then propagated updip to a weaker segment.

5 Conclusions

We performed the dynamic source inversion of the M_W7.1 Puebla-Morelos deadly earthquake close to Mexico City at intermediate depths. To this purpose we introduced a new Particle Swarm Optimization algorithm for determining some dynamic parameters of the rupture process following an elliptical source-geometry approximation and a slip-weakening friction law. Our results indicate that rupture was highly dissipative and remarkably slow. More than 84% of the available potential energy for the dynamic rupture propagation dissipated in the focal region. Considering the preexistent slab temperature and heat production associated with the estimated specific fracture energy, creation of pseudotachylytes (friction-induced melts) in the fault-zone is a plausible scenario enhancing rupture propagation. Despite the large dissipation, the source process generated very high accelerations in the fault (i.e. large excitation of short period waves), which contributed to the exceptionally-strong ground motion observed in the epicentral zone and Mexico City. Rupture directivity to the northwest could also have contributed to this observation. Similar and independent estimates of the rupture-energy balance for IDEs in different tectonic settings and geographies strongly suggest that slow, inefficient ruptures with remarkably high energy radiation may represent a preponderant universal feature of earthquakes at intermediate depths.

References

Andersen, T. B., Mair, K., Austrheim, H., Podladchikov, Y. Y., and Vrijmoed, J. C. (2008). Stress release in exhumed intermediate and deep earthquakes determined from ultramafic pseudotachylyte. *Geology* 36(12), 995-998.

Blum, C., and Li, X. (2008). Swarm intelligence in optimization. In Swarm Intelligence (pp. 43-85). *Springer*.

Braeck, S., and Podladchikov, Y. Y. (2007). Spontaneous thermal runaway as an ultimate failure mechanism of materials. *Physical Review Letters* 98, 095504.

Bouchon, M. (1981). A simple method to calculate Green's functions for elastic layered media. *Bulletin of the Seismological Society of America* 71(4), 959-971.

Campillo, M., Singh, S. K., Shapiro, N., Pacheco, J., and Hermann, R. B. (1996). Crustal structure south of the Mexican volcanic belt, base don group velocity dispersion. *Geofsica Internacional* 35(4).

Cocco, M., Spudich, P., and Tinti, E. (2006). On the mechanical work absorbed on faults during earthquake ruptures. In Radiated Energy and the Physics of Earthquakes Faulting. *AGU.*

Cruz-Atienza, V. M., Olsen, K. B., and Dalguer, L. A. (2009). Estimation of the breakdown slip from strong-motion seismograms: Insights from numerical experiments. *Bulletin of the Seismological Society of America*, 99(6), 3454-3469.

Cruz-Atienza, V.M., S. K. Singh, M. Ordaz (2017). ¿Qué ocurrió el 19 de septiembre de 2017 en México? *Revista del Colegio de Ingenieros Civiles de México*, 580, 20-24.

Dalguer, L. A., and Day, S. M. (2007). Staggeredgrid splitnode method for spontaneous rupture simulation. *Journal of Geophysical Research: Solid Earth* 112(B2).

Day, S. M., Dalguer, L. A., Lapusta, N., and Liu, Y. (2005). Comparison of finite difference and boundary integral solutions to threedimensional spontaneous rupture. *Journal of Geophysical Research: Solid Earth* 110(B12).

Díaz -Mojica, J., CruzAtienza, V. M., Madariaga, R., Singh, S. K., Tago, J., and Iglesias, A. (2014). Dynamic source inversion of the M6. 5 intermediatedepth Zumpango earthquake in central Mexico: A parallel genetic algorithm. *Journal of Geophysical Research: Solid Earth* 119, 7768-7785.

Di Carli, S., C. FrancoisHolden, S. Peyrat, and R. Madariaga (2010), Dynamic inversion of the 2000 Tottori earthquake based on elliptical subfault approximations, *J. Geophys. Res.* 115, B12328.

Di Toro, G., Nielsen, S., and Pennacchioni, G. (2005). Earthquake rupture dynamics frozen in exhumed ancient faults. *Nature*, 436(7053), 1009.

Eberhart, R., and Kennedy, J. (1995, October). A new optimizer using particle swarm theory. In Micro Machine and Human Science, 1995. MHS'95., Proceedings of the Sixth International Symposium on (pp. 39-43). IEEE.

Ferrand, T. P., Hilairet, N., Incel, S., Deldicque, D., Labrousse, L., Gasc, J., ... and Schubnel, A. (2017). Dehydration-driven stress transfer triggers intermediate-depth earthquakes. *Nature communications* 8, 15247.

Fulton, P. M., Brodsky, E. E., Kano, Y., Mori, J., Chester, F., Ishikawa, T., ... and Toczko, S. (2013). Low coseismic friction on the Tohoku-Oki fault determined from temperature measurements. *Science*, 342(6163), 1214-1217.

Frohlich, C. (2006). Deep earthquakes. *Cambridge university press*

García, D., Singh, S. K., Herráiz, M., Pacheco, J. F., and Ordaz, M. (2004). Inslab earthquakes of central Mexico: Q, source spectra, and stress drop. *Bulletin of the Seismological Society of America* 94, 789-802.

Green, H. W., and Houston, H. (1995). The mechanics of deep earthquakes. *Annual Review of Earth and Planetary Sciences* 23, 169-213.

Hacker, B. R., Peacock, S. M., Abers, G. A., and Holloway, S. D. (2003). Subduction factory 2. Are intermediatedepth earthquakes in subducting slabs linked to metamorphic dehydration reactions? *Journal of Geophysical Research: Solid Earth* 108.

Herrera C., S. Ruiz, R. Madariaga and P. Poli (2017). Dynamic inversion of the 2015 Jujuy earthquake and similarity with other intraslab events. *Geophys. J. Int.* 209, 866875.

Ida, Y. (1972). Cohesive force across the tip of a longitudinalshear crack and Griffith's specific surface energy. *Journal of Geophysical Research* 77(20), 3796-3805.

John, T., Medvedev, S., Rpke, L. H., Andersen, T. B., Podladchikov, Y. Y., and Austrheim, H. (2009). Generation of intermediate-depth earthquakes by self-localizing thermal runaway. *Nature Geoscience* 2, 137.

Jung, H., Green Ii, H. W., and Dobrzhinetskaya, L. F. (2004). Intermediate-depth earthquake faulting by dehydration embrittlement with negative volume change. *Nature* 428, 545.

Kanamori, H., Anderson, D. L., and Heaton, T. H. (1998). Frictional melting during the rupture of the 1994 Bolivian earthquake. *Science* 279, 839-842.

Kanamori, H., and Brodsky, E. E. (2004). The physics of earthquakes. *Reports on Progress in Physics* 67(8), 1429.

Manea, V. C., and Manea, M. (2011). Flat-slab thermal structure and evolution beneath central Mexico. *Pure and Applied Geophysics* 168(8-9), 1475-1487.

Marcinkovich, C., and Olsen, K. (2003). On the implementation of perfectly matched layers in a threedimensional fourthorder velocitystress finite difference scheme. *Journal of Geophysical Research: Solid Earth* 108(B5).

Melgar, D., PrezCampos, X., RamirezGuzman, L., Spica, Z., Espndola, V. H., Hammond, W. C., and CabralCano, E. (2018). Bend Faulting at the Edge of a Flat Slab: The 2017 Mw7. 1 PueblaMorelos, Mexico Earthquake. Geophysical Research Letters.

Mikumo, T., Olsen, K. B., Fukuyama, E., and Yagi, Y. (2003). Stress-breakdown time and slip-weakening distance inferred from slip-velocity functions on earthquake faults. *Bulletin of the Seismological Society of America*, 93(1), 264-282.

Nishitsuji, Y., and Mori, J. (2013). Source parameters and radiation efficiency for intermediate-depth earthquakes in Northeast Japan. *Geophysical Journal International* 196(2), 1247-1259.

Okuwaki, R., and Yagi, Y. (2017). Rupture process during the Mw 8.1 2017 Chiapas Mexico earthquake: shallow intraplate normal faulting by slab bending. *Geophysical Research Letters* 44, 816823.

Perry, M., Spinelli, G. A., Wada, I., and He, J. (2016). Modeled temperatures and fluid source distributions for the Mexican subduction zone: Effects of hydrothermal circulation and implications for plate boundary seismic processes. *Geochemistry, Geophysics, Geosystems* 17(2), 550-570.

Peyrat, S., and K. B. Olsen (2004), Nonlinear dynamic rupture inversion of the 2000 Western Tottori, Japan, earthquake, *Geophys. Res. Lett.* 31, L05604.

Poli, P., and Prieto, G. A. (2016). Global rupture parameters for deep and intermediatedepth earthquakes. *Journal of Geophysical Research: Solid Earth* 121(12), 8871-8887.

Prieto, G. A., Beroza, G. C., Barrett, S. A., Lpez, G. A., and Florez, M. (2012). Earthquake nests as natural laboratories for the study of intermediate-depth earthquake mechanics. *Tectonophysics*, 570, 42-56.

Prieto, G. A., Florez, M., Barrett, S. A., Beroza, G. C., Pedraza, P., Blanco, J. F., and Poveda, E. (2013). Seismic evidence for thermal runaway during intermediatedepth earthquake rupture. Geophysical Research Letters, 40(23), 6064-6068.

Prieto, G. A., Froment, B., Yu, C., Poli, P., and Abercrombie, R. (2017). Earthquake rupture below the brittle-ductile transition in continental lithospheric mantle. *Science Advances* 3, e1602642.

Ruiz, S., and Madariaga, R. (2013). Kinematic and dynamic inversion of the 2008 Northern Iwate earthquake. *Bulletin of the Seismological Society of America* 103(2A), 694-708.

Scambelluri, M., Pennacchioni, G., Gilio, M., Bestmann, M., Plmper, O., and Nestola, F. (2017). Fossil intermediate-depth earthquakes in subducting slabs linked to differential stress release. *Nature Geoscience* 10, 960.

Scholz, C. H. (1998). Earthquakes and friction laws. *Nature* 391, 37.

S.K. Singh, Mario Ordaz, Xyoli Pérez-Campos, and Arturo Iglesias (2015). Intraslab versus Interplate Earthquakes as Recorded in Mexico City: Implications for Seismic Hazard. *Earthquake Spectra* 31, 795-812.

S.K. Singh, E. Reinoso, D. Arroyo, M. Ordaz, V. M. Cruz-Atienza, X. Prez-Campos, A. Iglesias and V. Hjrleifsdttir. Deadly Intraslab Mexico Earthquake of 19 September 2017 (Mw7.1): Ground Motions and Damage Pattern in Mexico City. *Under review in Bull. Seismic. Soc. Am., April 2018.*

Suárez G., M. A. Santoyo, V. Hjorleifsdottir, A. Iglesias, C. Villafuerte and V. M. Cruz-Atienza. Large Scale Lithospheric Detachment of The Downgoing Cocos Plate: The 8 September 2017 Earthquake (Mw 8.2). *Under review in Nature Geoscience, January 2018.*

Suganthan, P. N. (1999). Particle swarm optimiser with neighbourhood operator. In Evolutionary Computation, 1999. CEC 99. *Proceedings of the 1999 Congress, IEEE*

Twardzik, C., Das, S. and Madariaga, R., 2014. Inversion for the physical parameters that control the source dynamics of the 2004 Parkfield earth- quake, *J. geophys. Res.* 119, 70107027.

Venkataraman, A., and Kanamori, H. (2004). Observational constraints on the fracture energy of subduction zone earthquakes. *Journal of Geophysical Research: Solid Earth, 109(B5).*